Manuscript 5253 – REVISION 1

Age, petrochemistry, and origin of a REE-rich mineralization in the Longs Peak - St. Vrain pluton near Jamestown, Colorado (USA)

Julien Allaz[1]*, Markus B. Raschke[2], Philip M. Persson[3], and Charles R. Stern[1]

[1] Department of Geological Sciences, University of Colorado Boulder, 399 UCB, Boulder, CO 80309

* Corresponding author: julien.allaz@colorado.edu

[2] Department of Physics, Department of Chemistry, and JILA, University of Colorado, Boulder, CO 80309, USA

[3] Department of Geology & Geological Engineering, Colorado School of Mines, 1516 Illinois Street, Golden CO 80401

Abstract

An unusual rare earth element (REE) mineralization occurs at a locality known as the "Rusty Gold" within the anorogenic 1.4 Ga Longs Peak - St. Vrain monzo- to syenogranite Silver Plume-type intrusion near Jamestown, Colorado (USA). Irregular shaped centimeter- to decimeter-sized mineralized pods and veins consist of zoned mineral assemblages dominated by fluorbritholite-(Ce) in a grey-colored core up to 10 cm thick, with monazite-(Ce), fluorite, and

minor quartz, uraninite, and sulfides. The core zone is surrounded by a black, typically millimeter-thick allanite-(Ce) rim, with minor monazite-(Ce) in the inner part of that rim. Bastnäsite-(Ce), törnebohmite-(Ce) and cerite-(Ce) appear in a thin intermediate zone between core and rim, often just a few hundreds of μm wide. Electron microprobe analyses show that the overall REE content increases from rim to core with a disproportionate increase of heavy REE (Σ_{HREE} increases 10-fold from 0.2 to 2.1%) compared to light REE (Σ_{LREE} increases 2-fold from 21.3 to 44.3%). The fluorbritholite-(Ce) contains minor U, Th, Fe, Mn, and Sr (total 0.10 apfu), with Al, Mg, Na, K, Ti, Pb, S and Cl below instrument detection limits. Cerite-(Ce) is a minor constituent of the thin zone between the inner rim and the core. The cerite-(Ce) is Fe-rich with low Ca, and minor Al, Mg and Mn, whereas törnebohmite-(Ce) is Al-rich and Ca-poor. Monazite-(Ce) and uraninite U-Th-Pb microprobe ages yield 1.420 (25) and 1.442 (8) Ga, respectively, confirming a co-genetic relationship with the host *ca.* 1.42 Ga Longs Peak - St. Vrain granite. We suggest the origin of the REE mineralization is a F-rich and lanthanide rich, either late-magmatic hydrothermal fluid or residual melt, derived from the granite. This late liquid, when becoming progressively enriched in REE as it crystallized, could explain the observed concentric mineralogical and geochemical zoning.

Keywords: Fluorbritholite-(Ce), Cerite-(Ce), Törnebohmite-(Ce), Allanite-(Ce), REE-speciation, Rusty Gold, peraluminous granite, Silver Plume, Colorado.

1. Introduction

This study focuses on the petrology and geochemistry of a particular Rare-Earth Element (REE) mineralization, and aims to fully describe and discuss possible REE enrichment processes that led to this mineral assemblage. This mineralization occurs as both veins and pods (ovoid or amoeboidal pockets) within aplitic dikes related to the 1.4 Ga Proterozoic Silver Plume-type anorogenic and peraluminous Longs Peak - St. Vrain granite near Jamestown, Colorado, USA (Fig. 1; Anderson and Thomas 1985). Goddard and Glass (1940) were the first to publish a description of this locality, known as the "Rusty Gold" deposit. They described the REE mineralization, including what they analyzed to be "cerite", "bastnäsite", and "allanite", as well as fluorite, quartz, uraninite, magnetite and sulfide phases, from several localities along the contact between pegmatite/aplite bodies and metasediment lenses (Figs. 1c, 2). A misidentification of the cerite-(Ce) was first suggested based on an XRD analysis (Rabbitt 1952), and this mineral was later confirmed to be fluorbritholite-(Ce) by *in situ* microanalysis (Affholter 1987; Affholter and Adams 1987) as it does not contain significant amounts of Fe or Al.

No such mineral assemblages associated with peraluminous granite as observed at this location have been reported in the literature from elsewhere in the world, and only a few papers discuss the occurrence of britholite-(Ce) and allanite-(Ce) with or without monazite-(Ce) in different geological contexts (e.g., Lira and Ripley 1990; Arden and Halden 1999; Hirtopanu et al. 2013). Despite its highly unusual mineralogical character, and its potential significance for the understanding of factors related to the concentration, transport and deposition of REE, this locality has not been investigated further since the works of Goddard and Glass (1940), Hanson and Pearce (1941), Rabbit (1952) and Gay (1957). In this paper, we present new whole-rock

63 analyses of the REE-rich veins, details of their mineral assemblages, their spatial zonal variation,
64 and electron microprobe analyses of the range of REE minerals they contain.
65

66 2. Geological Setting

67 The REE mineralization is related to the Longs Peak - St. Vrain pluton dated by Rb-Sr at 1.42(3)
68 Ga (Peterman et al. 1968; Peterman and Hedge 1968). This pluton is part of the Silver Plume-
69 type intrusions (Anderson and Thomas 1985), also known as the Berthoud Plutonic Suite (Tweto
70 1987). All these intrusions have been dated between 1.45 and 1.39 Ga (Peterman et al. 1968;
71 Stern et al. 1971). The Longs Peak - St. Vrain pluton was emplaced at shallow depth (0.2-0.3
72 GPa; Anderson and Thomas 1985). The presence of Paleoproterozoic xenoliths (mainly ~1.8 Ga
73 biotite schist; DePaolo 1981) further indicates that the studied outcrops are close to the margin of
74 the intrusion (Goddard and Glass 1940). Silver Plume-type intrusions are a series of anorogenic
75 (A-type) two-mica monzogranites to syenogranites exhibiting enrichment in K and other
76 incompatible elements (Rb, Sr, LREE), and depletion in Ca and Mg compared to orogenic
77 granites (Boos and Boos 1934; Wells 1967; Flanagan 1973; Baker et al. 1976).
78 $Al_2O_3/(CaO+Na_2O+K_2O)$ molecular ratios yield 1.03 to 1.27, hence the classification as
79 peraluminous granites (Anderson and Thomas 1985). The overall geochemistry suggests that the
80 source of this intrusion was the melting of garnet-rich high-grade quartzo-feldspathic continental
81 crust (DePaolo 1981; Anderson and Thomas 1985). In terms of REE content, data are scarce, but
82 suggest a strong enrichment in LREE (500-1000 times chondritic values) and a strong
83 fractionation of LREE to HREE with La_N/Yb_N ~72 (Flanagan 1973; chondrite-normalized ratios

using data from McDonough and Sun 1995), consistent with a garnet-bearing source (Flanagan 1973; Baker et al. 1976).

The study area is situated along the SE side of the Longs Peak - St. Vrain intrusion. Geological mapping reveals several pegmatite and aplite dikes associated with the intrusion (Cole and Braddock 2009; Fig. 1b). These dikes are sometimes in contact with lenses of Paleoproterozoic metasediments (1.7 Ga Idaho Springs group) that are included within the granite. Although 1.4 Ga deformation is documented locally in the region (e.g., Moose Mountain shear zone; Cole and Braddock 2009), the granite, pegmatites, aplite dikes and mineralized veins we studied do not appear to be deformed.

Goddard and Glass (1940) first described the occurrence of the REE-rich veins and pods within the aplite associated with the Longs Peak - St. Vrain granite at two localities near Jamestown, CO; a northern and a southern one [indicated by (1) and (2), respectively in Fig. 1b]. They identified two visually distinct mineral zones within the REE veins from the northern locality: a rim primarily composed of dark green to brown allanite-(Ce) with minor monazite-(Ce), and a core composed essentially of what they identified as “cerite” (>50% modal), a rare REE-silicate mineral, with fluorite (10-25%), and minor quartz. Bastnäsite-(Ce) and iron sulfides minerals were also identified. They noted that the southern locality contained, in addition, törnebohmite-(Ce), but no fluorite, and did not exhibit the rim/core structure characteristic of the northern locality. Both localities are significantly radioactive, due to minor actinides included in most REE minerals in trace to minor amounts as well as uraninite.

Goddard and Glass (1940) reported whole rock chemistry of the REE veins and pods with up to 56 weight-% total rare earth oxide (REO), including 28.85% Ce_2O_3 and 30.14% of the other REOs and Y_2O_3. They reported 2.94% Y_2O_3 (+ heavy REO), with 0.28% ThO_2, and 0.51%

107 U_3O_8. They estimated "cerite" and allanite-(Ce) compositions using whole rock chemistry and
108 mineral modal abundances. Hanson and Pearce (1941) further extended the mineral analyses of
109 cerite-(Ce) and allanite-(Ce) using wet chemical analysis. Gay (1957) provided an X-ray
110 diffraction analysis. The misidentification of fluorbritholite-(Ce) as "cerite" was suggested by
111 Rabbit (1952) and Affholter (1987).
112

113 # 3. Sample description& petrography

114 ## *3.1 Sample collection*

115 Samples from both the northern and southern localities (Fig. 1c) were collected from outcrop,
116 including three drill cores of ca. 0.3, 0.5, and 1.2 meters each from the northern locality, and
117 float material (Fig. 2a). The focus of this study is on the more complex northern locality (outcrop
118 1; Fig. 1b), where the relation between aplite and the REE mineralization is clearly visible at the
119 outcrop (Fig. 2b). No outcrop could be identified at the southern locality (locality 2; Fig. 1b).
120 The float samples collected there were found to be mostly allanite-(Ce)-bearing, and do not seem
121 to be representative of the samples collected by Goddard and Glass (1940).

122 The observed REE-mineralization at the northern locality is restricted to the aplite. The
123 aplite consists of highly variable feldspar content (15-50% plagioclase, 30-70% K-feldspar),
124 quartz (5-20%) and minor biotite. Grain size in the aplite is variable from 0.2 to 0.6 mm. The
125 contact of the REE-mineralization with the aplite from the northern locality is sharp at the
126 outcrop scale (Fig. 2a-c). The REE mineralization is generally 1-5 cm in size, and forms pods
127 with ovoid to amoeboidal geometry and without any apparent gradational zone with the aplite
128 (Fig. 2a,b). The largest pods found reach up to *ca.* 30 cm in size. Additionally, REE

mineralization occurs as 1-10 centimeter-thick veins or elongated pods (Fig. 2c) that can be followed over several decimeters, along with numerous 1-2 mm thick dark green veinlets isolated in the aplite and essentially composed of allanite-(Ce). These veins and veinlets anastomose within the aplite (Fig. 2b,d) and commonly crosscut each other.

The mineralization consists of REE-silicate, phosphate, and minor carbonate minerals. Two major mineral zones are readily identified in the thicker veins or pods: a black rim and a dark-gray core (Fig 2a-c). Grain sizes are larger in the rim, and visible with a hand lens, with a pronounced decrease in grain size in the core. Fresh core areas often appear violet-colored due to abundant 20-100 μm fluorite grains in the REE pods and veins. Weathered surfaces of the core appear light greenish and are more susceptible to erosion, compared to the black rim. Locally an irregular submillimeter- to millimeter-size yellowish area made of fine-grain minerals, including REE-carbonates, has been observed between the core and rim on freshly cut samples.

Three representative samples A2, A4, and B1 used for most of the petrographic observations and *in situ* samples were collected from the northern locality (outcrop 1; Fig. 1c). Minimal surface exposures preclude detailed study of the structure or extent of the mineralization at depth. Most observations thus rely on the cores drilled at several locations and on float material dug from prospect trenches at this locality, where the mineralization is observed over a surface area of *ca.* 100x100 meters.

3.2 Petrography

Four concentric zones were recognized in the REE-rich veins based on mineral assemblages observed in thin section. These zones are labeled #1 to #4 from rim to core. Intermediate zone #3 is not always present and occurs between the central core zone #4 and the inner rim zone #2. Due

to the small grain size (typically 20-100 μm), fine intergrowth, and low modal abundance of some mineral phases, optical mineral identification remains difficult in thin section (Fig. 3). Therefore, mineral identification relied on electron microprobe analysis, using backscattered electron (BSE) imaging, qualitative EDS, WDS X-ray mapping, and quantitative mineral analysis. Figure 4 summarizes the phases identified by EDS. Mineral formulas for each REE-phase are listed in Table 1 and a summary of each mineral zone is given in Table 2.

3.2.1 Rim minerals (zones #1 & #2)

Zone #1 is a 1-3 mm outer rim, largely monomineralic, and composed of allanite-(Ce) (Fig. 3; Table 2). Its contact with the aplite is sharp (no transition zone) and regular to strongly amoeboidal at thin section scale (Fig. 3a,b). Few host rock minerals (e.g., quartz, feldspar) are found in this zone. Millimeter-sized veinlets of allanite-(Ce) crosscutting existing mineralization (Fig. 2a) or penetrating the host rock (Fig. 2d) are also observed, as are isolated 100-200 μm allanite-(Ce) crystals within the aplite.

Prismatic euhedral allanite-(Ce) crystals are typically 50-200 μm long and 20-50 μm wide (Fig. 3c,d). C-axes of allanite-(Ce) crystals in direct contact with the aplite are commonly oriented perpendicular to the contact with the host rock (Fig. 3b,c). As observed by Goddard and Glass (1940), crystals close to the aplite contact tend to be more green, whereas grains towards the inside of the vein are more brownish to dark-brown (Fig. 3b,c). Individual grains also exhibit a faint concentric zonation in their pleochroism and birefringence.

Zone #1 gradationally transitions into an inner rim zone #2 still dominated by allanite-(Ce) and containing up to 20% modal abundance monazite-(Ce), and rarely quartz. Monazite-(Ce) crystals are 20-80 μm sub-euhedral to anhedral clear grains, with high birefringence.

Monazite-(Ce) is present throughout zones #2 to 4 in a relatively constant modal abundance (Table 2).

3.2.2 Intermediate zone minerals (zone #3)

Törnebohmite-(Ce) and cerite-(Ce) (Table 1) are chiefly found in a thin intermediate zone #3 along with the REE-carbonates [bastnäsite-(Ce) ± synchysite-(Ce)], in a zone devoid of fluorite. Compared to fluorbritholite-(Ce), cerite-(Ce) is colorless, shows a similar birefringence [dark gray for cerite-(Ce), light gray to white for fluorbritholite-(Ce)], and exhibits uniaxial positive [negative for fluorbritholite-(Ce)] birefringence. Note that this is distinct from the description of the minerals thought to be cerite-(Ce) by Goddard and Glass (1940): their description of "cerite" refers to minerals in the core region, which is chiefly composed of fluorbritholite-(Ce) (see below). Törnebohmite-(Ce) and REE-carbonates can be differentiated from both fluorbritholite-(Ce) and cerite-(Ce) by their higher birefringence [up to second order green for törnebohmite-(Ce) and third to fourth order for bastnäsite-(Ce)]. This zone is typically only 100-200 μm wide (rarely up to 500 μm), with crystal sizes around 20-100 μm. Minor and small (<20μm) allanite-(Ce) and fluorbritholite-(Ce) grains may also be present.

3.2.3 Core minerals (zone #4)

The core zone #4 is composed of a fine-grained, nearly equigranular intergrowth of fluorbritholite-(Ce), monazite-(Ce), fluorite, quartz, and minor uraninite (Table 2). Minerals in the core are mostly isogranular with a constant 120° dihedral angle at triple junction between all major phases [fluorbritholite-(Ce), monazite-(Ce), quartz and fluorite].

Fluorbritholite-(Ce) dominates the core zone, occurring as 20-80 μm equigranular grains with no preferred crystallographic orientation. It can be distinguished from the other minerals by its greenish color in plane polarized light and its low birefringence (grey). Monazite-(Ce) shares similar habits as described in zone #2. Locally, millimeter-sized nodules composed exclusively of fluorite and monazite-(Ce) and surrounded by pyrite are found within the core zone (Fig. 5). Fluorite is present only in the core zone (Table 2). It is typically deep purple at the crystal rim and sometimes with a colorless core, and exhibits sub-euhedral cubic sections. Crystal size is usually 10-60 μm. Late fractures cutting straight through the core and rim zones commonly contain larger fluorite crystals (100-200 μm). Some larger fluorite grains are associated with quartz, and form secondary veins crossing the core zone. Quartz is omnipresent in the core in 50-150 μm grains. Larger crystals up to 1 mm are possible in late veins crossing the REE-mineralization (Fig. 3b). Accessory phases in the core include uraninite, bastnäsite-(Ce),and sulfides (pyrite, chalcopyrite, and rare sphalerite and galena). Sparse micron-sized uraninite grains (<5 μm) are present everywhere within the core zone, whereas bastnäsite-(Ce) occurs very rarely as isolated grains or as 20-50 μm veinlets. Pyrite and chalcopyrite appear to be concentrated either with "nodules" of fluorite and monazite-(Ce) or as grains within late fluorite + quartz veins crossing the REE-mineralization. Late alteration within the intermediate and core zones (#3 and #4) is visible along cracks. This alteration is characterized by an abundance of high-birefringence minerals (REE-carbonate), smaller grains size (10-20 μm), and greenish-yellow coloration at the outcrop scale (Fig. 2b), which appears grayish-black in thin section (Fig. 3b).

4. Analytical methods

4.1 Bulk composition of the vein

Six REE-rich vein samples were used for bulk rock major, minor, and trace element compositional analysis (ActLabs, Inc., Ontario, Canada). Prior to crushing, samples were trimmed with a saw to remove all surrounding aplitic material, leaving only the vein sample. Each sample was approximately 100g, and was crushed and prepared by ActLabs using a mild steel mill. The samples included five from veins, one of which consists of both core and rim combined (REE4), while the other four are of the core only (REE5-8). One additional allanite-(Ce)-rich sample was also analyzed from the southern locality (REE9). The analysis of major elements was obtained by fusion ICP, and trace elements by ICP (Ba, Be, Sc, Sr, V, Y, Zr) or ICP-MS (other trace elements). Fluorine was measured by ion-selective electrodes method.

4.2 Electron microprobe analysis

Mineral analyses and X-ray element mapping were performed on three samples (A2, A4, and B1) from the northern outcrop by WDS using a JEOL JXA-8600 electron microprobe at the University of Colorado-Boulder. It is a four-spectrometer instrument equipped with an argon X-ray detector (P-10 mixture) on spectrometer 1 and 2 (PET and TAP crystals), and xenon X-ray detector on spectrometers 3 and 4 (LiF crystals). Operating conditions using a W-cathode were 25 keV, and 20 nA beam current for most mineral phases. A higher current of 50 nA was used for allanite-(Ce) and uraninite to reduce the detection limits. A defocused beam (5 to 10 μm diameter) was used whenever possible for hydrous or fluorine bearing phases to minimize beam damage. No evidence of beam damage was observed under these conditions for all but the REE-

carbonates. For these minerals, a 10 nA current and 10 μm beam diameter was used. A larger beam size was not possible for the REE-carbonates due to their small grain size, and a lower current would have increased the detection limit of several elements (especially HREE) to unacceptable levels. Details of the analytical setup including standards, X-ray lines, and analysis time for each element are listed in Supplementary Table 1a; beam current used for each analysis is provided with the complete analysis results (Supplementary Table 2). Background positions were adequately chosen to avoid interferences (Supplementary Table 1a). Peak interference corrections were applied for (1) Ce $M\zeta$ on F $K\alpha$, (2) Nd $L\alpha$ *(II)* on Cl $K\alpha$, (3) Dy$L\alpha$ on Eu$L\beta$, (4) Ho $L\alpha$ on Gd $L\beta$, (5) Tb $L\beta$ on Er $L\alpha$, (6) Sm $L\gamma$, Gd $L\beta_2$ and Dy $L\beta_{1,4}$ on Tm $L\alpha$, and (7) Th $M\zeta$ on U $M\beta$. The duration per analysis for each setup was 10 minutes (see Supplementary Table 1 for counting time for each element). Only analyses with totals between 98 and 102% were retained, except for the REE-carbonate for which a good analysis was difficult to obtain due to the small grain size and the high beam sensitivity. Values below detection limits were removed from the results.

4.3 Electron microprobe dating of monazite-(Ce) and uraninite

Additional monazite-(Ce) analyses were performed with the Cameca SX-100 "Ultrachron" at the University of Massachusetts, Amherst to obtain electron U-Th-Pb microprobe ages along with full quantitative analyses. Five individual crystals in two areas within the core zone #4 of sample A2 were selected. Analytical conditions were 15 keV, 200 nA beam current, focused beam diameter of 1 μm, and counting times for U, Pb and Th of 400, 500 and 250 seconds, respectively. In addition to U, Th and Pb, monazite-(Ce) analyses include Si, P, S, Ca, As, Y and REE (La to Nd and Sm to Yb). Uraninite analyses were obtained with a JEOL JXA-8600

instrument at the University of Colorado-Boulder, using a 50 nA beam current, a focused beam, and a similar setup for other element analysis as described above (Supplementary Table 1c). All major interference corrections for REE and actinide elements were applied to ensure accurate analysis, especially for U and Pb analysis (Th $M\gamma$ on U $M\beta$; Y $L\gamma$; La $L\alpha$ and Th $M\zeta$ on Pb $M\alpha$; see Allaz et al. 2013). U-Th-Pb dates were calculated based on the age equation from Montel et al. (1996) and decay constants from Steiger and Jäger (1977). Standardization and age calculations for monazite-(Ce) were checked for consistency before and after each analysis session using the standard Moacyr monazite. The 2σ errors reported include counting statistics and a 10% relative error on the background regression. Details of the monazite-(Ce) analysis setup can be found in Allaz et al. (2013), with the difference being that the multipoint background method was employed. This method permits precise determination of the background curvature and accurate measurement of the background under U $M\beta$, Th $M\alpha$ and Pb $M\alpha$ on monazite-(Ce) by measuring 3 to 5 backgrounds on either side of each peak (Supplementary Table 1b; Allaz et al., 2014). The background characterization for U-Th-Pb analysis in uraninite was less crucial, as all these elements are present as major elements; a classical two-point background acquisition was used with off-peak position adequately chosen to avoid background interferences.

5. Results

5.1 Bulk composition of the vein

Results of bulk rock analysis from the six REE vein samples are presented in Table 3, and the resulting normalized REE and trace element diagrams are shown in Figure 6. The samples of the core of four veins (REE5-8), one of which has high modal fluorite (high F and CaO), and of the core and rim of one other (REE4) vein from the northern locality, are all significantly enriched in total REE (40 to 46%). In particular, LREE is $>10^5$ times chondritic abundance and $>10^3$ times the concentration of LREE in 1.4 Ga Silver Plume-type intrusions (Fig. 6). A significant fractionation of HREE to LREE is observed, with La_N/Yb_N ratios between 94 and 124. The slope between LREE and HREE flattens towards the HREE, with Dy_N/Yb_N ratio between 3.1 and 3.3. Only the allanite-(Ce)-rich sample (REE9) from the southern locality differs significantly, with lower total REE but with a higher La_N/Yb_N ratio of 511 (Dy_N/Yb_N = 3.4). This is actually expected, as the sample from the southern locality is nearly monomineralic and only representative of the allanite-(Ce)-rich rim (zone #1 and #2). Therefore sample REE9 does not represent the typical REE-mineralization observed at the northern outcrop, and is only used to compare the bulk composition of the allanite-(Ce)-rich rim versus the bulk compositions of the vein samples (REE4-8) dominated by a fluorbritholite-(Ce)-rich core. All REE-patterns in the studied mineralization display only a weak negative Eu-anomaly ($Eu^* = Eu_N/[0.5*(Sm_N+Gd_N)]$ = 0.80), whereas the Longs Peak - St. Vrain granite shows a strong negative Eu-anomaly (Eu* = 0.33).

Some other incompatible elements also show significant enrichment compared to Silver Plume-type intrusions (Fig. 6b) that indicate a strongly fractionated character of the mineralization. Sc and Lu each reach 50-60 ppm, Sr 1480-2550 ppm, Th 2410-3240 ppm, and U

3160-4180 ppm in the veins. Although Goddard and Glass (1940) did not detect P in their samples, P_2O_5 contents in our samples range from 3.7 to 4.8%, consistent with the significant modal abundance of monazite-(Ce), as well as minor P_2O_5 in fluorbritholite-(Ce) (see §5.2). In contrast to other incompatible elements, Ba, Rb, and K are depleted in veins compare to Silver Plume-type intrusions. A strong negative Ti anomaly is also apparent in the veins (Fig. 6b).

5.2 Mineral chemistry

Electron microprobe analyses of minerals from three samples A2, A4, and B1 from the northern locality are presented here in the order of primary occurrence within the veins from rim to core. In addition to quartz and fluorite, EDS revealed the presence of allanite-(Ce), monazite-(Ce), törnebohmite-(Ce), cerite-(Ce), Ca-free and Ca-bearing REE-carbonates [bastnäsite-(Ce) and bastnäsite-(Ce)± synchysite-(Ce)/parisite-(Ce)], fluorbritholite-(Ce), and uraninite (Table 1; Fig. 4). Additionally, several X-ray WDS element maps were acquired (1) to reveal possible intra-grain zonation, and (2) to highlight the different mineral assemblages, which can be difficult to recognize due to the small grain size and the similarity in optical properties of some phases. Composite red-green-blue (RGB) X-ray element maps using Si-La-Ca (Fig. 7a-c) and Ca-Al-C (Fig. 7d,e) were chosen to distinguish the individual REE phases. The compositions of each REE-phase are summarized in Table 4 (complete data set available in Supplementary Table 2). In general, all REE minerals are found to be Ce-dominant, followed by La and Nd. Only cerite-(Ce), fluorbritholite-(Ce) and uraninite yield a higher Nd-content compared to La, up to the extreme case where the Nd-content of uraninite is identical to its Ce-content within the uncertainty of the analysis. The following discussion highlights a few key points about the composition of each of the REE-rich minerals. Additional information on mineral formula

normalization (recalculation of water content and oxidation state of Fe) is given in the supplementary document.

Allanite-(Ce) is the only mineral showing strong intra-grain compositional zoning, clearly visible in BSE images, and correlated with variable REE-content (Fig. 8a-c). Mineral formula recalculation following recommendation from Ercit (2002) allows for vacancies at the A site (occupied normally by Ca and REE), and permits an estimate of Fe^{3+}/Fe^{2+} content based on charge balance (Table 4, Supplementary Table 2). As expected from the petrographic observations and the browner coloration of grains close to the core of the REE vein, allanite-(Ce) from mineral zone #2 is richest in REE (average 27.3% RE_2O_3). Similarly, the largest allanite-(Ce) crystal in zone #1 and the isolated crystal in the aplite show both concentric variation in pleochroic color and birefringence and significant variation in REE content (Fig. 8c,d). The detailed study of a 100 μm grain in zone #1 of sample A2 (Fig. 8c) shows three major domains: (1) a relatively REE-poor core (21.7% RE_2O_3), (2) a small inner domain with a high concentration of REE (26.5% RE_2O_3), and (3) a rim with intermediate and slightly variable REE content (23.8-25.3% RE_2O_3). Allanite-(Ce) from zone #2 shows minor compositional variation and the largest REE content (26.8-27.6% RE_2O_3) compared to allanite-(Ce) from zone #1, as suggested by the relatively homogeneous BSE signal (inset of Figure 8b). Figure 9 depicts the overall variations of composition considering Fe^{2+}-Fe^{3+} recalculated by charge balance and assuming Mn as Mn^{2+}. The latter assumption might be erroneous and some Mn^{3+} could be present (Supplementary Figure 1; see discussion in supplementary document). Overall, this mineral is classified as allanite-(Ce), although it contains a significant component of ferriallanite-(Ce), dissakisite-(Ce), and a minor Mn-component [maganiandrosite-(Ce), khristovite-(Ce) or

piemontite; see mineral formula in Table 1 and discussion of allanite-(Ce) zoning in supplementary material].

Monazite-(Ce) compositions in all zones #2 to #4 are fairly homogeneous with only small intragrain compositional variations (Table 4, Supplementary Table 2). Only a slight increase in ThO_2 content (0.5 to 1.7%) is observed at the very rim of some grains (Fig. 10a), and is correlated with an increase in Si and Ca [minor cheralite-(Ce) and thorite substitution]. UO_2 content is constant around 0.1%. Despite the low actinide content, U-Th-Pb_{total} dating of several grains within the core zone #4 yields consistent results between 1.38(2)Ga and 1.47(3)Ga (2σ error; average of 6 to 8 single analyses), with no correlation with the minor compositional variation. Results are represented using Gaussian probability distributions, and yield an overall average age of 1.420(25) Ga (Fig. 10b).

Törnebohmite-(Ce) is fairly homogeneous with a considerable Al_2O_3 (10.0%) and minor Fe, Mg, and Ca (Table 4, Supplementary Table 2). Only minor variation in LREE, Al, Fe and Cl content is observed (e.g., two average compositions in Table 4). Minor amounts of P_2O_5were detected in a few grains (<0.27% P_2O_5). Small compositional variation occurs chiefly between La+Ce and the other REE (+ Ca, U, Th; Fig. 11a). In sample A4, törnebohmite-(Ce) grains found in zone #3 appears to be slightly richer in Nd, Sm and other HREE compared to rare grains found in the interior of the core zone #4 (Fig. 11a). Fluorine content remains low and often below detection limit. Chlorine is usually below detection limit except in a few grains close to a late quartz vein (Fig. 7e), where Cl content ranges from below detection limit up to 0.16%.

Cerite-(Ce) composition is Fe-rich (2.0-3.4% Fe_2O_3) with some CaO (2.4%), and minor Al_2O_3 (0.3%), Mn_2O_3 (0.3%), MgO (0.2%) and SrO (<0.2%; Table 4, Supplementary Table 2). The low Al- and high Fe-content makes cerite-(Ce) distinct from fluorbritholite-(Ce). HREE

content is low, below or close to the detection limit for most HREE, but some samples contain significant Y_2O_3 (1.8-3.5%), and detectable Dy_2O_3 (0.1-1.0%) and Er_2O_3 (0.06-0.3%). Cerite-(Ce) can accommodate 4 to 7 OH-groups both in ferrian cerite-(Ce) or aluminocerite-(Ce) (Table 1; Moore and Shen 1983; Nestola et al. 2009). However, the uncertainty due to lack of OH-content analysis does not affect the REE partitioning. Small but clearly identifiable variations mainly in REE, Al, Fe, and Mn content occur between different cerite-(Ce) grains. Ce and La are positively correlated, yet together anti-correlated with other REE. Fe, Al, Mn, and Mg are anti-correlated. The sum of divalent cations (Ca, Mg and Sr) remains low and is slightly correlated with the total REE content (Fig. 12b).

Ca-free REE-carbonate, identified as **bastnäsite-(Ce)** (Fig. 12c), is present in trace amount in the core zone #4. No analysis yielded a good total, all being around 95 and 96% including CO_2 and H_2O recalculated by stoichiometry (Table 4, Supplementary Table 2). Nonetheless, oxygen-based mineral formula recalculation yields a value close to 1 cation (even for a few analyses obtained at 20 or 50 nA), suggesting that the proportion of REE measured is correct (Table 4, Supplementary Table 2). Fluorine dominates the OH-site with 0.6 to 1.0 apfu.

A few **Ca-bearing REE-carbonates** detected by EDS (Fig. 4) are present within the intermediate zone #3 and in late veins (e.g., Fig. 7e). Due to the small grain size, alteration, and inclusions, the analyses results are not satisfactory (Table 4, Supplementary Table 2). Calcium content is variable and low (1.5-2.8% CaO), far from the ideal composition of parisite-(Ce) (10.4% CaO) or synchysite-(Ce) (17.6% CaO). Totals of these analyses tend to be too high (97.8 to 103.0%), with abnormally high concentrations of SiO_2, Al_2O_3 or P_2O_5, which stem from interference from fine grained inclusions of other silicates, monazite-(Ce), and fluorite.

EDS spectrum in **uraninite** (Fig. 4) reveals a high U and Pb peak with significant amount of REE and Th. Assuming a structural formula as depicted in Janeczek and Ewing (1992) and Evron et al. (1994; Table 1), oxidation of uranium (U^{4+} or U^{6+}) due to the introduction of divalent and trivalent cations can be recalculated. Despite this calculation, totals are still slightly low (95.1-98.9%; Table 4, Supplementary Table 2), which can be explained by the small grain size (often <5μm), the presence of elements not analyzed, or possible metamictization (alteration). Uraninite is the only REE-bearing mineral with equal amounts of Ce_2O_3 (5.1%) and Nd_2O_3 (5.0%) and with a relatively high Y content (1.5% Y_2O_3) compare to the total REO content (16.1% RE_2O_3). A significant amount of Th (2.2% ThO_2) and Pb (14.2% PbO) was measured, which, as for monazite-(Ce), permits the determination of U-Th-Pb_{total} age (e.g., Bowles 1990; Hurtado et al. 2007); 11 individual analyses in 11 grains from samples A2 and A4 yield an average of age of 1.442(8) Ga (Table 4, Supplementary Table 2).

Finally, the core zone #4 is essentially composed of **fluorbritholite-(Ce)** (70% modal). Fluorbritholite-(Ce) is distinguished from cerite-(Ce) or törnebohmite-(Ce) by a large concentration of CaO (10.9%) along with the very low content of Fe_2O_3 and Mn_2O_3 (each <0.7%), and undetectable concentrations of Al_2O_3 and MgO (Table 4, Supplementary Table 2). OH sites are dominated by F. Britholite-(Ce) is part of the apatite supergroup (general formula $A_5T_4O_{12}X$; A = Ca, REE; T = Si, P; X = OH, F, Cl). In contrast to apatite, in which the T-site is mostly filled with P, the large concentration of Si at the T-site of fluorbritholite-(Ce) (Fig. 11d) can accommodate a large concentration of REE that typically exceeds Ca at the A site (Noe et al. 1993; Oberti et al. 2001). Analyses reported here are similar to previous analyses by Affholter (1987; WDS analysis) and Kartashov (EDS analysis; mindat.org website), although the latter two only reported a limited number of analyzed elements (Table 4). Our analyses reveal a higher

418 HREE content in fluorbritholite-(Ce) compared to most other REE phases analyzed (4.3%
419 Y_2O_3+HRE_2O_3; Fig. 11e). Small variations mainly in LREE and HREE content between the
420 three analyzed samples are observed. A significant concentration of P_2O_5 was detected (0.2-
421 1.2%) and is anti-correlated with SiO_2, which reflects the apatite-britholite solid solution. For
422 additional discussion on fluorbritholite-(Ce) compositional zoning see supplementary material.
423

424 # *6.* Discussion

425

426 ## *6.1 Rare minerals*

427 Our microprobe analyses show that the main REE mineral phase, which had originally been
428 described as "cerite" by Goddard and Glass (1940) is instead fluorbritholite-(Ce) (mineral
429 formula in Table 1), as was suggested by Rabbit (1952), Affholter (Affholter 1987; Affholter and
430 Adams 1987), and Kartshov (mindat.org website, 2011). Only minor cerite-(Ce) actually exists
431 in the studied samples. Few reports of fluorbritholite exist in the literature, likely due to the fact
432 that F is not always analyzed. Jiexiang et al.(1994) first described fluorbritholite-(Ce) from its
433 type locality in nepheline syenite at Mont St-Hilaire, Canada (Mandarino 1996). To the best of
434 our knowledge, no fluorbritholite-(Ce) occurrence has yet been described that exhibits an
435 identical mineral assemblage, texture, and geological setting of the type encountered near
436 Jamestown. The most similar occurrence is associated with the Eden Lake Complex in Manitoba,
437 Canada (monzonite granite; Arden and Halden 1999), where the occurrence of britholite-(Ce)
438 and allanite-(Ce) in late pegmatitic segregations is reported. According to the reported F-content
439 in britholite-(Ce) (2.15 to 3.25%), it should in fact be considered as fluorbritholite-(Ce).

440 However, the occurrence of allanite-(Ce) and fluorbritholite-(Ce) with significant aegerine-
441 augite, titanite and apatite, but without monazite-(Ce), in their study area differs from the mineral
442 assemblages at Jamestown. Whereas the Jamestown mineralization is associated with an
443 anorogenic peraluminous granite intrusion (two-mica monzo- to syenogranite), the few other
444 known localities with fluorbritholite are associated with alkaline (e.g., Della Ventura et al. 1999;
445 Liferovich and Mitchell 2006; Pekov et al. 2007), peralkaline (agpaitic; e.g., Jiexiang et al. 1994;
446 Sørensen 1997), and carbonatite intrusions (e.g., Feldman et al. 1987). Pekov et al. (2007)
447 describe the mineral and its holotype occurrence on Mount Kukisvumchorr in the Kola Peninsula
448 in Russia, where it appears as veinlets in fenitized gneiss xenoliths. Agpaitic intrusions, such as
449 the Mont St-Hilaire Complex in Canada (e.g., Jiexiang et al. 1994), are also known for their
450 primary REE-mineralization, which includes fluorbritholite-(Ce) and rare Na-rich REE minerals.
451 Fluorbritholite-(Ce) was also identified in skarn-related occurrences in the Bergslagen mining
452 region of Sweden (Holtstam and Andersson 2007) as well as in a carbonatite from Nam Nam Xe
453 in Vietnam (Feldman et al. 1987). Other alkali-syenite rocks are the host of britholite-(Ce),
454 particularly as a secondary mineral (e.g., Della Ventura et al. 1999; Liferovich and Mitchell
455 2006). These later studies report a high F-content in britholite-(Ce), and therefore this mineral
456 should properly be considered fluorbritholite-(Ce).

457 Törnebohmite-(Ce) is also an uncommon REE-silicate mineral, with less than 20
458 occurrences described (e.g., Shen and Moore 1982; Bonazzi et al. 2003; Holtstam et al. 2003;
459 Hirtopanu et al. 2013). Its occurrence at Jamestown is scarce, mainly occurring in zone #3 at the
460 interface between the allanite-(Ce) rim and the fluorbritholite-(Ce)-rich core, and more rarely in
461 the core zone #4. It is accompanied in zone #3 by cerite-(Ce), in itself another rare REE-mineral
462 occurring in pegmatite associated with peraluminous granite (Förster 2000), in carbonatite or

463 metasomatized metamorphic rocks (Glass et al. 1958; Belolipetkii and Voloshin 1996), in syenite
464 pegmatite (Larsen 1996), or in the Bastnäs-type skarn deposit in Sweden (Holtstam and
465 Andersson 2007). Large variations in Al, Fe, Mg and Ca content have been reported. Moore and
466 Shen (1983) first described cerite-(Ce) as an Mg-rich REE-silicate from Bastnäs (Sweden).
467 Later, additional cerite-group species were described: Al-rich cerite-(Ce) from Erzgebirge
468 (Germany; Förster 2000), Fe-rich cerite-(La) from the Kola Peninsula (Russia; Pakhomovsky et
469 al. 2002), and aluminocerite-(Ce) from Baveno (Italy; Nestola et al. 2009). Ca-content varies,
470 and is typically less than 1 apfu in cerite-(Ce) and cerite-(La) (Pakhomovsky et al. 2002;
471 Holtstam and Andersson 2007), and up to 3 apfu in aluminocerite-(Ce) (Nestola et al. 2009).
472 Based on these papers, the cerite-(Ce) observed in Jamestown should be classified as a new iron-
473 dominant species of cerite-(Ce) with 0.54-0.71 apfu Fe^{3+}, 0.74-0.80 apfu Ca, 0.07-0.17 apfu Al,
474 0.06-0.11 apfu Mg, and 0.03-0.09 apfu Mn^{3+}, which could be named "ferricerite-(Ce)".
475

476 ***6.2 REE partitioning among minerals***

477 REE-patterns of all REE-bearing minerals were compared using chondrite normalization (Fig.
478 12; McDonough and Sun 1995). Monazite-(Ce), allanite-(Ce) and törnebohmite-(Ce)show the
479 strongest partitioning between LREE and HREE (HREE/REE apfu ratio ≤0.03; Table 4,
480 Supplementary Table 2; Fig. 12a-c).The total REE content increases from allanite-(Ce) to
481 törnebohmite-(Ce) to monazite-(Ce). Fluorbritholite-(Ce) and cerite-(Ce) exhibit enrichment in
482 HREE with a lower ratio of LREE to HREE (HREE/REE apfu ratio 0.04 to 0.09; Table 4,
483 Supplementary Table 2 and Fig. 12c,d). As fluorbritholite-(Ce) dominates the core zone #4,
484 REE-pattern of this mineral resembles the one from whole rock analyses of most veins (compare
485 Figs. 5a and 15e), with a slightly lower normalized HREE content in the whole rock analysis of

REE-veins due to the presence of LREE-rich monazite-(Ce) (12% modal; Table 2). Similarly, the whole rock analysis of an allanite-(Ce)-rich rim from the southern locality matches closely the allanite-(Ce) REE pattern (compare Figs. 5a and 15b). Uraninite from core zone #4 shows the least fractionation between LREE and HREE with a hump around Nd-Sm (Fig. 12d) and the highest HREE/REE ratio (0.15-0.24) of all REE-bearing minerals. In addition to a high REE content (ca. 16.2% RE_2O_3), uraninite is also rich in ThO_2 (*ca.* 2.2% ThO_2; Table 4, Supplementary Table 2). Such a composition and REE-pattern is consistent with a high-temperature origin of this mineral related to residual liquid (fluids or melt) derived from the magmatic intrusion (e.g., Frimmel et al., 2014; Mercadier et al. 2011). The presence of additional REE minerals with uraninite [fluorbritholite-(Ce) and monazite-(Ce)] is likely to constrain the REE pattern of uraninite. The hump around Nd and Sm might result from the preferential incorporation of LREE (especially Ce and La) in monazite-(Ce) causing the depletion at the time of uraninite growth of the mineralizing fluid (or melt) in Ce and La.

The partitioning of REE in Ca-free and Ca-bearing REE carbonate follows two trends (Fig. 12e). Pure bastnäsite-(Ce) occurs as grains in apparent textural equilibrium within the core zone #4. Its REE pattern is similar to monazite-(Ce) or törnebohmite-(Ce). The Ca-bearing bastnäsite-(Ce) is interpreted as a sub-micron interlayer of pure bastnäsite-(Ce) and either synchysite-(Ce) or parisite-(Ce) (e.g., Ruberti et al. 2008), or fluorite. The REE-pattern in Ca-bearing bastnäsite-(Ce) follows more closely the one for fluorbritholite-(Ce) or cerite-(Ce). Its close association with alteration domains within the core zone #4 (late vein) or close to the intermediate zone #3 and the REE pattern both suggest that it is a secondary alteration product of fluorbritholite-(Ce) or cerite-(Ce). Local alteration of allanite-(Ce) to bastnäsite-(Ce) within the

aplite is also observed (Fig. 8d), although the small grain size and close association with allanite-(Ce) prevented microprobe analysis.

The enrichment of fluorbritholite-(Ce), uraninite and cerite-(Ce) in HREE compared to other minerals reflects a progressive REE fractionation process from a mineral assemblage with high LREE/HREE ratio at the rim zones [#1 and #2; allanite-(Ce)and monazite-(Ce)] to minerals with lower LREE/HREE in the core zone #4. Figure 13 shows this effect in a Ce/Nd versus Ce/Y plot. This enrichment in Y and HREE is accompanied by a decrease in Ce and La, and an increase in Nd and Sm in minerals such as fluorbritholite-(Ce), uraninite and cerite-(Ce). Allanite-(Ce), cerite-(Ce) and fluorbritholite-(Ce) are the main phases that show compositional variation, and these compositional zonations also depict a change in HREE vs. LREE content, as indicated by correlated decrease in the two ratios Ce/Nd and Ce/Y (Fig. 13). In the case of allanite-(Ce), this variation occurs within each grain of zone #1, with an increasing REE content towards the rim, and a slight depletion in Y and Nd towards allanite-(Ce) from zone #2 (Fig. 13). In the case of fluorbritholite-(Ce), this variation occurs locally, inter- or intra-sample. The few analyses of uraninite are mostly homogeneous with a strong enrichment in Nd, Sm and Y+HREE, and with the lowest Ce/Nd and Ce/Y ratios.

Nonetheless, the overall HREE content remains relatively low and does not permit the formation of HREE-dominant minerals such as xenotime-(Y) or britholite-(Y). The small but significant amount of HREE identified in the bulk composition is partitioned preferentially in fluorbritholite-(Ce) and to a minor extent in cerite-(Ce) and uraninite, i.e., in the vein core minerals.

In general, Silver Plume-type intrusions are strongly enriched in LREE and show a strong partitioning of LREE to HREE (Fig. 6; Flanagan 1973; Baker et al. 1976). A striking difference

between the REE partitioning of Silver Plume-type intrusions and the mineralization is the absence of a strong Eu-anomaly in the mineralization (Fig. 6). This feature currently remains unexplained. The partitioning of Eu depends on several factors such as oxygen fugacity, fractionation (notably crystallization of plagioclase), and melt composition and structure (e.g., Möller and Muecke 1984). We can only speculate that the F-enrichment in the aplitic and mineralizing fluid (or melt) might have resulted in a preferential partitioning of Eu in the REE mineralization along with all other REE: the oxygen fugacity could have been also high enough to prevent reduction of Eu.

Similarities between the REE pattern of Silver Plume-type intrusions and the REE mineralization observed at Jamestown (Fig. 6) suggest that the source of the REE is the magmatic intrusion. A co-genetic relationship between a magmatic-derived fluid and REE-mineralization is not uncommon (e.g., Lira and Ripley 1990, 1992; Agangi et al. 2010; Hirtopanu et al. 2013). For comparison, pegmatites from the South Platte district in A-type the Pikes Peak batholith present a high overall enrichment in HREE with minerals such as samarskite-(Y) and xenotime-(Y) (Simmons and Heinrich 1980). However in this case, the associated granite composition shows a less-pronounced fractionation of LREE and HREE, and an overall higher HREE content (Simmons et al. 1987; Beane and Wobus, 1999; Smith et al. 1999). Although the granite composition appears to be a primary factor to constrain the observed mineral assemblages in the studied REE mineralization, the specifics of the F-rich magmatic liquid composition could also control the evolution of the REE mineralization observed at Jamestown as discussed below.

6.3 Petrogenesis of the vein

The timing of mineralization is constrained by the monazite-(Ce) and uraninite U-Th-Pb_{total} electron microprobe dating, which yield respectively 1.420(25) and 1.442(8) Ga. As the Longs Peak - St. Vrain pluton is dated by Rb-Sr at 1.42(3) Ga (Peterman et al. 1968), we conclude that the mineralization occurs during or shortly after pluton emplacement. The significant presence of pegmatite and aplite in the studied area together with several meter- to hectometer-sized slices of metasediment xenoliths from the surrounding Paleoproterozoic metapelitic rock (~1.7 Ga) within the pluton further suggests that the intrusive rocks near Jamestown represent the margin of the pluton at relatively shallow depth (0.2-0.3 GPa; Anderson and Thomas 1985), possibly close to the roof of the pluton (Goddard and Glass 1940).

Apart from their overall enrichment in REE, a key petrogenetic element of the REE mineralization from Jamestown is the concentric zoning within the pods and veins as described above. Several millimeter-sized veins within the aplite matrix are exclusively composed of allanite-(Ce), whereas other mineralization occurs in pods or larger veins with a rim composed of allanite-(Ce) (±monazite-(Ce); zone #1 and #2), transitioning to a very thin intermediate zone containing a törnebohmite-(Ce) and cerite-(Ce) assemblage (zone #3), and finally a core zone of fluorbritholite-(Ce) and monazite-(Ce), with quartz and significant modal fluorite (zone #4). Figure 14 sketches the suggested formation of the REE mineralization within pods, which is developed in the following.

The occurrence of allanite-(Ce) can possibly be seen as a reaction product between the REE-mineral pods and surrounding silicates (feldspar, quartz, ±biotite). Goddard and Glass (1940) suggested that allanite-(Ce) from Jamestown is a replacement texture. In a study on allanite-(Ce) and britholite-(Ce) segregation within pegmatite, Arden and Halden (1999) also

576 suggested that allanite-(Ce) originates from a replacement reaction between REE-rich fluid and
577 silicates from pegmatite. Pan and Fleet (1990) discussed the growth of halogen-bearing allanite-
578 (Ce) associated with a calcium-silicate alteration zone (skarn) with inverse zoning similar to the
579 one observed in Jamestown (increase REE from core to rim). Although in the case of Jamestown
580 a skarn (*sensu stricto*) can be excluded due to the absence of carbonaceous rocks, the aplite is
581 rich in plagioclase (An0.26-0.33; Supplementary Table 2) and shows evidence for late
582 albitization with altered rims around An0.04-0.09. However, our detailed mineral chemistry and
583 petrology data do not support growth of allanite-(Ce) from a reaction between REE-rich minerals
584 and silicate from the aplite, because: (1) allanite-(Ce) occurs as veins or isolated crystals within
585 the aplite, without fluorbritholite-(Ce), and with a very similar zoning (Figs. 2d, 8d), (2) allanite-
586 (Ce) commonly grows perpendicular to the contact with the host rock in pods (Fig. 3b,c), (3)
587 most allanite-(Ce) crystals are perfectly euhedral, and (4) no remnant of possible reactants [e.g.,
588 fluorbritholite-(Ce), cerite-(Ce), törnebohmite-(Ce), plagioclase] are found within the allanite-
589 (Ce)-rich domain. It is also difficult to reconcile a reaction between fluorbritholite-(Ce) and
590 aplitic material, as this would involve a strong change in chemistry (metasomatism), with a
591 preferential loss of HREE [allanite-(Ce) having a stronger partitioning of LREE to HREE], and
592 enrichment in Fe and minor Mg and Mn. Breakdown of törnebohmite-(Ce) and monazite-(Ce)
593 could produce allanite-(Ce), as their REE patterns are more similar (Fig. 12a-c). Hirtopanu et al.
594 (2013) suggested such a reaction in REE mineralization associated with an alkaline intrusion
595 complex. However, this in unlikely in the case of Jamestown as (1) törnebohmite-(Ce) and
596 monazite-(Ce) occur in such small quantities in the samples from Jamestown, (2) no relic
597 törnebohmite-(Ce) within allanite-(Ce) was found, (3) monazite-(Ce) coexists with allanite-(Ce)
598 within zone #2, and (4) the question of the source of Fe enrichment remains as pyrite (in aplite

599 and in the mineralization) and biotite (in aplite only) are minor constituents of the overall
600 assemblage.

601 We propose instead that allanite-(Ce) is a first growth stage within the pods and veins
602 precipitating from either a high temperature magmatic fluids or a residual melt ("liquid" in
603 Figure 14a,b), and not a replacement texture. Allanite-(Ce) crystals from the rim zone #1 are
604 zoned from REE-poor core to REE-richer rim, whereas allanite-(Ce) from zone #2 is relatively
605 homogeneous and shows the highest REE content (Figs. 8, 9), which according to our
606 interpretation reflects either a change in liquid composition (progressive enrichment in REE)
607 and/or change in environmental conditions (pressure, temperature, pH and redox conditions;
608 Gieré 1996). The early growth of allanite-(Ce) instead of fluorbritholite-(Ce) suggests that the
609 magmatic fluid or residual melt was not only rich in REE, but also in Si, Al, Fe, and Ca. This
610 interpretation would then be similar to the occurrence described by Lira and Ripley (1990) of
611 britholite-(Ce), allanite-(Ce) [partially replaced by bastnäsite-(Ce)] and fluorite in nodules in
612 hydrothermally altered rocks (fenite) associated with biotite monzogranite. Their study suggests
613 a cogenetic growth of allanite-(Ce) and britholite-(Ce), or with allanite-(Ce) growing shortly
614 after britholite-(Ce), due to a moderate salinity magmatic fluid of high temperature (356-535 ºC).

615 The coexistence of allanite-(Ce) (LREE-silicate) and monazite-(Ce) (LREE-phosphate)
616 characterize zone #2 (Fig. 14c). Such a coexistence is unusual in "common" rocks with only
617 trace REE such as felsic intrusive and (meta-)sedimentary rocks, as allanite-(Ce) and monazite-
618 (Ce) are known to be stable under different conditions (e.g., Janots et al. 2008). The stability
619 field of allanite-(Ce) is normally restricted to medium temperature, possibly co-existing with
620 apatite, whereas monazite-(Ce) grows either at very low metamorphic grade or at higher
621 temperature following the breakdown of allanite-(Ce) (e.g., Pan et al. 1994; Finger et al. 1998;

622 Wing et al. 2003; Janots et al. 2008; Hirtopanu et al. 2013). Broska et al. (2000) reported the
623 presence of both monazite-(Ce) and allanite-(Ce) in peraluminous granite, but not in equilibrium.
624 Pan and Fleet (1990) suggested a co-genetic growth of monazite-(Ce), allanite-(Ce) and apatite
625 in skarn. In the context of the REE-rich veins from Jamestown, both allanite-(Ce) and monazite-
626 (Ce) show no sign of resorption, and we suggest that the hydrothermal nature of the
627 mineralization, the supersaturation of LREE and the presence of small amount of P in the
628 magmatic liquid, together with a high Si, Al and Fe content, accounts for this unusual co-genetic
629 growth. Monazite-(Ce) requires very low P saturation to grow (0.02-0.05% P_2O_5; Wolf and
630 London 1995) and the REE content along with additional extrinsic condition (notably pressure
631 and temperature) is most likely the key factor preventing earlier growth of monazite-(Ce).

632 A thin zone of törnebohmite-(Ce) and cerite-(Ce) precede the fluorbritholite-(Ce)-rich
633 core. Minerals from this zone are essentially unique to the intermediate zone #3, except for
634 törnebohmite-(Ce), which is locally found in the core zone. Bastnäsite-(Ce) (pure or Ca-bearing)
635 can be present in variable amounts in this intermediate zone (compare zone #3a and #3b in
636 Figure 7a,d,e). Only trace amounts of pure bastnäsite-(Ce) are present in the core zone #4, and
637 minor cerite-(Ce) is only present at the very edge of the core zone (Fig. 7b-e). The coexistence of
638 törnebohmite-(Ce) and cerite-(Ce) might be of primary origin (Fig. 14d), following the allanite-
639 (Ce) and monazite-(Ce) growth. If correct, this implies the liquid became progressively enriched
640 in HREE and depleted in Fe and Al, as cerite-(Ce) is clearly HREE-richer compared to allanite-
641 (Ce) and monazite-(Ce) (Fig. 12a-c). Alternatively, törnebohmite-(Ce), cerite-(Ce) and REE-
642 carbonate could represent a reaction product between allanite-(Ce) and fluorbritholite-(Ce)
643 (evolution from Figure 14e to f). Indeed, the REE-pattern of cerite-(Ce) resembles that of
644 fluorbritholite-(Ce) (Fig. 12c,d; Fig. 13), whereas the törnebohmite-(Ce) REE pattern lies

between those of allanite-(Ce) and monazite-(Ce) (Fig. 12b,c; Fig. 13). The presence of relics of fluorbritholite-(Ce) and allanite-(Ce) within zone #3 (Fig. 7b) and some cerite-(Ce) in zone #4 close to the contact with zone #3 (Fig. 7d,e) supports this idea.

The last stage of crystallization is composed essentially of fluorbritholite-(Ce), fluorite, monazite-(Ce), quartz and minor uraninite (Fig. 14e,f). The presence of fluorite and quartz implies that F and Si both reached saturation point. The purple coloration especially at the rim of fluorite is most likely the effect of radioactivity (e.g., Braithwaite et al. 1973). Affholter and Adams (1987) suggested that fluorbritholite-(Ce) and törnebohmite-(Ce) resulted from the breakdown of allanite-(Ce), but several lines of evidence disprove this. First, fluorbritholite-(Ce) chemistry is significantly richer in HREE compared to any other minerals, especially allanite-(Ce), which shows a less pronounced partitioning of LREE and HREE. Second, törnebohmite-(Ce) is limited to the intermediate zone #3 and only rarely present in the core zone #4 (e.g., Fig. 7c), whereas the proposed reaction would require a 1:1 proportion of fluorbritholite-(Ce) and törnebohmite-(Ce). Third, the proposed reaction from Affholter and Adams (1987) requires the production of anorthite and magnetite to balance the release of Fe, Al and Ca from allanite-(Ce) breakdown, none of which is observed with the mineralization. These elements might be balanced by the production of cerite-(Ce) (Fe, Al, ±Ca), törnebohmite-(Ce) (Al), sulfide (Fe) and Ca-bearing REE-carbonate, but the modal abundance of these minerals in the mineralization is too low. Instead, we suggest that the core zone #4 represents the final crystallization stage of a more fractionated liquid enriched in HREE, which evolved from the magmatic liquid. The fine grain size suggests that the crystallization occurred rapidly, possibly due to a rapid change in temperature as the REE-rich liquids rose from their source towards the cooler roof of the pluton, or a rapid change in liquid condition (e.g., pH, redox conditions). We cannot exclude that the

mineralization has suffered some level of recrystallization to produce the isogranular texture of the core minerals, which is unusual for hydrothermal mineralization. However, if this happened, it had to occur shortly after the crystallization as both uraninite and monazite-(Ce) yield ages within the error of the intrusion age.

The petrogenetic history of the REE mineralization at Jamestown shows some other minor additional complexities worth noting. Late allanite-(Ce)-rich veins are locally present, along with quartz and fluorite veins (±sulfide), and reflect some late fluid-rock interaction after the crystallization of the main REE mineral pods and veins. The late allanite-(Ce)-rich veins crosscutting existing mineralization suggest either multiple mineralization events or remobilization of the REE mineralization (dissolution-reprecipitation). Finally, nodules composed of monazite-(Ce) and fluorite, and surrounded by Fe-sulfide minerals are observed within the core zone #4. Such a texture could be the results of late pockets of immiscible liquid supersaturated in F, P and S.

6.4 Implications for REE-speciation

The mineral assemblages and chemistry of the individual REE phases provides some insight into the transport, concentration and deposition of REE in peraluminous granites. The abundance of F in most REE minerals strongly suggests that the transport of primary REE minerals was controlled by complexation of REE with OH and F. Numerous studies have highlighted the high capacity of F-rich fluid to transport and concentrate REE and other high field strength elements based either on field observations and petrology (e.g., Pan and Fleet 1990; Banks et al. 1994; Pan and Fleet 1996; Agangi et al. 2010; Hirtopanu et al. 2013) or on laboratory experiments (e.g., Webster 1990; Wood 1990; Keppler 1993; Haas et al. 1995; Webster et al. 2004).

Whereas our primary hypothesis relies on the existence of a hydrothermal fluid, we cannot exclude the possibility of a late magmatic liquid extracted from the Longs Peak - St. Vrain granite, and possibly the formation of two immiscible residual melts; a silica-rich and a fluorine-rich melt. The Si-rich melt could be responsible for the formation of the aplite, whereas the F-rich melt would preferentially partition all REE (e.g., Vasyukova and Williams-Jones 2014). Indeed, our preliminary fluid inclusion study in the REE mineralization revealed an *absence* of primary fluid inclusions, and the presence of rounded fluorine inclusions notably in quartz. Moreover, a fast crystallizing residual melt would be more compatible with the fine equigranular texture observed in the core of the mineralization and two immiscible residual melts could account for the amoeboidal contact between the aplite and the mineralization (Figs. 2, 3). More work on fluid inclusions and possible melt inclusions in both the aplite and the mineralization is required.

The high-F content of the mineralization suggest similarities in term of transportation and precipitation with the work of Agangi et al. (2010 and reference therein). This latter study investigated REE concentration in felsic magmas (rhyolites); we suggest that the REE concentration, transport and deposition history in Jamestown followed a similar path: (1) the residual felsic melt extracted from the pluton is enriched in fluorine, (2) the crystallization of major silicate minerals in the granite and/or aplite (quartz, feldspar, ±biotite) without F-rich phases further enriched the residual melt in F, and forced a liquid phase (fluid or melt) enriched in REE to exsolve (e.g., Webster 1990), (3) which subsequently concentrated in pods and along cracks (veins), and lastly (4) REE-rich phases sequentially crystallized from this liquid. As the initial REE-bearing phase [allanite-(Ce)] crystallized in the residual melt, the final liquid became

more strongly enriched in REE (e.g., London et al. 1988; Webster et al. 2004), leading to the mineralization sequence as discussed above.

Studies on REE speciation in high-temperature fluids emphasize the strong complexation of REE, especially HREE, with fluorine and to a lesser degree with chlorine (e.g., Wood 1990; Haas et al. 1995); REE also appear to fractionate strongly in F-rich melt during the formation of two immiscible silicate–fluoride melts (Vasyukova and Williams-Jones 2014). With the complexation decreasing with decreasing temperature, and based on our petrographic observations and microprobe analyses, we conclude that the zoned mineral assemblage can be explained by increasing saturation of LREE in the magmatic liquid (fluid or melt) through progressive cooling. The inverse compositional zoning (REE-poor core; Fig. 8) observed in allanite-(Ce) within the aplite, in isolated allanite-(Ce) veins and at the rim of larger REE-mineral pods represents the onset of this LREE saturation in the residual magmatic liquid. This process is correlated with the general increases in HREE (compare to LREE) as observed from the rim to the core of the mineralization. This change is accompanied by a progressive undersaturation of Fe and reduced Al activity that prevents further crystallization of allanite-(Ce) and enables monazite-(Ce) crystallization. The intermediate mineral assemblage in zone #3 further supports this decrease in Al and Fe saturation in the remaining liquid, as cerite-(Ce) and törnebohmite-(Ce) are still Fe- and Al-bearing, respectively, but with a much lower content compared to allanite-(Ce). The HREE enrichment observed in the core of the REE mineralization could be explained by the preferential partitioning of HREE in the residual magmatic F-rich liquid (Haas et al. 1995) until the temperature decreased to a threshold where all REE were supersaturated, or until the liquid condition changed (e.g., lowering of the F activity after fluorite

735 crystallization). Indeed, the presence of significant quantities of quartz and fluorite in the core of
736 the mineralization (zone #4) suggests that Si and F content in the liquid became supersaturated.
737 The mineralogy further suggests the presence of additional ligands such as PO_4^{3-}
738 (monazite), Cl [minor constituent in some törnebohmite-(Ce) crystals], SO_4^{2-} (minor sulfides and
739 significant concentration of SO_3 in monazite), or CO_2 [bastnäsite-(Ce)]. CO_2 activity during the
740 primary crystallization phase of the REE mineralization may have remained low, as only small
741 amounts of pure bastnäsite-(Ce) are present (<0.5% modal). The CO_2-bearing liquid possibly
742 only affected the late stage of mineralization in a significant way, e.g., during alteration and late
743 remobilization of the first phase of REE-mineralization. The liquid was likely to be low in
744 salinity, as chlorine is often below detection limit in the hydrous and fluorine-rich phases.
745 However, the role of these additional ligands and their combined effect cannot be discussed
746 conclusively in this study, and it is clear from the amount of fluorite in the core of the Jamestown
747 pods and veins, that F-rich liquid was the main factor in producing this unusual REE
748 mineralization.
749
750

751 # Acknowledgments

752 We thank P. Emery, T. Nystrom, and H. Scott from the Balarat Outdoor Education Center,
753 Denver Public Schools for providing site access. The Smithsonian Institution/National Museum
754 of Natural History gratefully provided REE phosphate standards used for electron microprobe
755 analysis (standards NMNH-168484 [$CePO_4$], and NMNH-168487 to NMNH-168499 [$EuPO_4$ to
756 $YbPO_4$, YPO_4]) and some silicate standards. We thank J.M. Montel and M.J. Jercinovic for

757 providing additional REE-phosphate standards ($LaPO_4$, $PrPO_4$, $NdPO_4$ and $SmPO_4$). JA would
758 like to acknowledge M.J. Jercinovic and M.L. Williams for granting access to the Cameca SX-
759 100 “Ultrachron” for monazite dating work. We thank S. Staude, D. London, W. B. Simmons,
760 and L.A. Groat for their helpful reviews at different stages of the manuscript. Additional help
761 from the associate editor D. Baker is acknowledged. The work is supported by USGS Mineral
762 Resource External Research Program grant #G14AP00052.

Bibliography

Affholter, K.A. (1987) Synthesis and crystal chemistry of lanthanide allanites, 222 p., PhD thesis, Virginia Polythechnic Institute and State University.

Affholter, K.A. and Adams, I.W. (1987) Thermal breakdown of allanite to britholite. GSA Abstracts with Programs, 19, 567.

Agangi, A., Kamenetsky, V.S., and McPhie, J. (2010) The role of fluorine in the concentration and transport of lithophile trace elements in felsic magmas: Insights from the Gawler Range Volcanics, South Australia. Chemical Geology, 273, 314–325.DOI: 10.1016/j.chemgeo.2010.03.008

Allaz J., Jercinovic M.J., Williams M.L., and Donovan J.J. (2014) Trace element analyses by EMP: Pb-in-monazite and new multipoint background method, Microscopy and Microanalysis, 20 (supplement 3), 720-721. DOI: 10.1017/S1431927614005327

Allaz, J., Selleck, B., Williams, M.L., and Jercinovic, M.J. (2013) Microprobe analysis and dating of monazite from the Potsdam Formation, New York: A progressive record of chemical reaction and fluid interaction. American Mineralogist, 98(7), 1106-1119. DOI: 10.2138/am.2013.4304

780 Anderson, J.L. and Thomas, W.M. (1985) Proterozoic anorogenic two-mica granites: Silver
781 Plume and St. Vrain batholiths of Colorado. Geology, 13(3), 177-180. DOI: 10.1130/0091-
782 7613(1985)13<177:PATGSP>2.0.CO;2

783 Arden, K.M. and Halden, N.M. (1999) Crystallization and alteration history of Britholite in
784 Rare-Earth-Element-enriched pegmatitic segregations associated with the Eden Lake
785 Complex, Manitoba, Canada. The Canadian Mineralogist, 37, 1239-1253.

786 Baker, F., Hedge, C.E., Millard, H.T.J., and O'Neil, J.R. (1976) Pikes Peak batholith:
787 geochemistry of some minor elements and isotopes, and implications for magma genesis. In
788 Professional Contributions of Colorado School of Mines, Studies in Colorado Field
789 Geology 8, p. 44-56.

790 Banks, D.A., Yardley, B.W.D., Campbell, A.R., and Jarvis, K.E. (1994) REE composition of an
791 aqueous magmatic fluid: A fluid inclusion study from the Capitan Pluton, New Mexico,
792 U.S.A. Chemical Geology, 113, 259–272.

793 Beane, R. and Wobus, R.A. (1999) Petrogenesis of the Sugarloaf syenite, Pikes Peak batholith,
794 Colorado. Rocky Mountain Geology, 34(2), 313-324. DOI: 10.2113/34.2.313

795 Belolipetkii, A.P. and Voloshin, A.V. (1996) Yttrium and rare earth element minerals from the
796 Kola Peninsula, Russia. In A. P. Jones, F. Wall, and C. T. Williams, Eds., Rare Earth
797 minerals: chemistry, origin and ore deposits, p. 311-326. Chapman & Hall, London, U.K.

798 Bonazzi, P., Bindi, L., and Parodi, G. (2003) Gatelite-(Ce), a new REE-bearing mineral from
799 Trimouns, French Pyrenees: Crystal structure and polysomatic relationships with epidote
800 and törnebohmite-(Ce). American Mineralogist, 88, 223-228.

801 Boos, M.F. and Boos, C.M. (1934) Granites of the Front Range - The Longs Peak-St. Vrain
802 batholith. Geological Society of America Bulletin, 45, 303-332.

803 Bowles, J.F.W. (1990) Age dating of individual grains of uraninite in rocks from electron
804 microprobe analyses.Chemical Geology, 83, 47-53.

805 Braithwaite, R.S.W., Flowers, W.T., Haszeldine, R.N., and Russel, M. (1973) The cause of the
806 colour of Blue John and other purple fluorites. Mineralogical Magazine, 39, 401–411.

807 Broska, I., Petrík, I., and Williams, T. (2000) Coexisting monazite and allanite in peraluminous
808 granitoids of the Tribeč Mountains, Western Carpathians. American Mineralogist, 85, 22-
809 32.

810 Cole, J.C. and Braddock, W.A. (2009) Geologic Map of the Estes Park 30’ x 60’ Quadrangle,
811 North-Central Colorado, 56 p. U.S. Geolological Survey Scientific Investigations Map
812 3039, 1 sheet, scale: 1:100,000, pamphlet.

813 Della Ventura, G., Williams, C.T., Cabella, R., Oberti, R., Caprilli, E., and Bellatreccia, F.
814 (1999) Britholite-hellandite intergrowths and associated REE-minerals from the alkali-
815 syenitic ejecta of the Vico volcanic complex (Latium, Italy): petrological implications
816 bearing on REE mobility in volcanic systems. European Journal of Mineralogy, 11, 843-
817 854.

DePaolo, D.J. (1981) Neodymium isotopes in the Colorado Front Range and crust-mantle evolution in the Proterozoic. Nature, 291, 193–196.

Ercit, T.S. (2002) The mess that is "allanite". Canadian Mineralogist, 40, 1411-1419. DOI: 10.2113/gscanmin.40.5.1411

Evron, R., Kimmel, G., and Eyal, Y. (1994) Thermal recovery of self-radiation damage in uraninite and thorianite. Journal of Nuclear Material, 217, 54–66.

Feldman, L.G., Sarkisyan, S. S., Boriskin, V. P., Purusova, S. P., Nguen, V. H., and Chin, S. Ben. (1987) Crystalline beckelite from Nam Se deposit (N Vietnam). Mineral. Zhurnal, 9(1), 78-86 (in Russian).

Finger, F., Broska, I., Roberts, M.P., and Schermaier, A. (1998) Replacement of primary monazite by apatite-allanite-epidote coronas in an amphibolite facies granite gneiss from the eastern Alps. American Mineralogist, 83, 248-258.

Flanagan, F.J. (1973) 1972 values for international geochemical reference samples. Geochimica et Cosmochimica Acta, 37, 1189-1200. DOI: 10.1016/0016-7037(73)90055-0

Förster, H.-J. (2000) Cerite-(Ce) and thorian synchysite-(Ce) from the Niederbobritzsch granite, Erzgebirge, Germany: Implications for the differential mobility of the LREE and Th during alteration. The Canadian Mineralogist, 38, 67-79. DOI: 10.2113/gscanmin.45.5.1073

Frimmel, H.E., Schedel, S., and Brätz, H. (2014) Uraninite chemistry as forensic tool for provenance analysis. Appl. Geochemistry 48, 104–121. DOI: 10.1016/j.apgeochem.2014.07.013

838 Gay, P. (1957) An X-Ray Investigation of some rare-earth silicates: Cerite, Lessingite, Beckelite,
839 Britholite, and Stillwellite. Mineralogical Magazine, 31(237), 455-468. DOI:
840 10.1180/minmag.1957.031.237.04

841 Gieré, R. (1996) Formation of rare earth minerals in hydrothermal systems, *in*: Jones, A.P., Wall,
842 F., Williams, C.T. (Eds.), Rare Earth Minerals: Chemistry, Origin and Ore Deposits.
843 Chapman & Hall, London, U.K., London, U.K., pp. 105–150.

844 Glass, J.J., Evans, H.T.J., Carron, M.K., and Hildebrand, F.A. (1958) Cerite from Mountain Pass,
845 San Bernardino County, California. American Mineralogist, 43, 460-475.

846 Goddard, E.N. and Glass, J.J. (1940) Deposits of radioactive cerite near Jamestown, Colorado.
847 American Mineralogist, 25(6), 381-404.

848 Haas, J.R., Shock, E.L., and Sassani, D.C. (1995) Rare earth elements in hydrothermal systems:
849 Estimates of standard partial molal thermodynamic properties of aqueous complexes of the
850 rare earth elements at high pressures and temperatures. Geochimica et Cosmochimica Acta,
851 59(21), 4329-4350. DOI: 10.1016/0016-7037(95)00314-P

852 Hanson, R.A. and Pearce, D.W. (1941) Colorado cerite. American Mineralogist, 26(2), 110-120.

853 Hirtopanu, P., Andersen, J.C., Fairhurst, R.J., and Jakab, G. (2013) Allanite-(Ce) and its
854 associations, from the Ditrau Alkaline Intrusive Massif, East Carpathians, Romania.
855 Proceedings of the Romanian Academy, Series B, 15, 59–74.

856 Holtstam, D. and Andersson, U.B. (2007) The REE minerals of the Bastnäs-type deposits, South-
857 Central Sweden. The Canadian Mineralogist, 45(5), 1073-1114. DOI:
858 10.2113/gscanmin.45.5.1073

859 Holtstam, D., Andersson, U.B., and Mansfeld, J. (2003) Ferriallanite-(Ce) from the Bastnäs
860 deposit, Västmanland, Sweden. The Canadian Mineralogist, 41, 1233-1240. DOI:
861 10.2113/gscanmin.41.5.1233

862 Hurtado, J.M., Hodges, K. V., and Bowring, S.A. (2007) Electron microprobe chemical dating of
863 uraninite as a reconnaissance tool for leucogranite geochronology. Nature Precedings. DOI:
864 10101/npre.2007.655.1.

865 Janeczek, J. and Ewing, R.C. (1992) Structural formula of uraninite. Journal of Nuclear
866 Materials, 190, 128–132.

867 Janots, E., Engi, M., Berger, A., Allaz, J., Schwarz, J.-O., and Spandler, C. (2008) Prograde
868 metamorphic sequence of REE minerals in pelitic rocks of the Central Alps; implications
869 for allanite-monazite-xenotime phase relations from 250 to 610 degrees C. Journal of
870 Metamorphic Geology, 26(5), 509-526. DOI: 10.1111/j.1525-1314.2008.00774.x

871 Jiexiang, G., Chao, G.Y., and Tang, S. (1994) Fluorbritholite-(Ce) A new mineral from Mont St.
872 Hilaire, Quebec, Canada. Journal of Wuhan University of Technology (China), 9(3), 9-14
873 (in Chinese with English abstract).

874 Keppler, H. (1993) Influence of fluorine on the enrichment of high field strength trace elements
875 in granitic rocks. Contributions to Mineralogy and Petrology, 114, 479–488.

Larsen, O.A. (1996) Rare Earth minerals from the syenite pegmatites in the Oslo region, Norway. In A. P. Jones, F. Wall, and C. T. Williams, Eds., Rare Earth minerals: chemistry, origin and ore deposits, p. 151-166. Chapman & Hall, London, U.K.

Liferovich, R.P. and Mitchell, R.H. (2006) Apatite-group minerals from nepheline syenite, Pilansberg alkaline complex, South Africa. Mineralogical Magazine, 70(5), 463-484. DOI: 10.1180/0026461067050346

Lira, R. and Ripley, E.M. (1990) Fluid inclusion studies of the Rodeo de Los Molles REE and Th deposit, Las Chacras Batholith, Central Argentina. Geochimica et Cosmochimica Acta, 54, 663–671.

Lira, R., and Ripley, E.M. (1992) Hydrothermal alteration and REE-Th mineralization at the Rodeo de Los Molles deposit, Las Chacras batholith, central Argentina. Contributions to Mineralogy and Petrology, 110, 370–386.

London, D., Hervig, R.L., and Morgan, G.B. (1988) Melt-vapor solubilities and elemental partitioning in peraluminous granite-pegmatite systems: experimental results with Macusani glass at 200 MPa. Contributions to Mineralogy and Petrology, 99, 360–373.

Mandarino, J.A. (1996) Abstracts of New Mineral Descriptions. Mineralogical Record, 27(6), 463-466.

McDonough, W.F. and Sun, S.-s. (1995) The composition of the Earth. Chemical Geology, 120, 223-253. DOI: 10.1016/0009-2541(94)00140-4

Mercadier, J., Cuney, M., Lach, P., Boiron, M.-C., Bonhoure, J., Richard, A., Leisen, M., and Kister, P. (2011) Origin of uranium deposits revealed by their rare earth element signature. Terra Nova, 23, 264–269.

Möller, P. and Muecke, G.K. (1984) Significance of Europium anomalies in silicate melts and crystal-melt equilibria: a re-evaluation. Contributions to Mineralogy and Petrology, 87, 242–250. DOI: 10.1007/BF00373057

Montel, J.-M., Foret, S., Veschambre, M., Nicollet, C., and Provost, A. (1996) Electron microprobe dating of monazite. Chemical Geology, 131, 37–53.

Moore, P.B. and Shen, J. (1983) Cerite, $RE_9(Fe^{3+},Mg)(SiO_4)_6(SiO_3OH)(OH)_3$: its crystal structure and relation to whitlockite. American Mineralogist, 68, 996-1003.

Nestola, F., Guastoni, A., Camara, F., Secco, L., Dal Negro, A., Pedron, D., Beran, A. (2009) Aluminocerite-Ce: A new species from Baveno, Italy: Description and crystal-structure determination. American Mineralogist, 94, 487–493. DOI:10.2138/am.2009.3060.

Noe, D.C., Hughes, J.M., Mariano, A.N., Drexler, J.W., and Kato, A. (1993) The crystal structure of monoclinic britholite-(Ce) and britholite-(Y). Zeitschrift für Kristallographie, 206, 233-246. DOI: 10.1524/zkri.1993.206.Part-2.233

Oberti, R., Ottolini, L., Della Ventura, G., and Parodi, G. (2001) On the symmetry and crystal chemistry of britholite: New structural and microanalytical data. American Mineralogist, 86, 1066-1075.

Pakhomovsky, Y.A., Men'shikov, Y.P., Yakovenchuk, V.N., Ivanyuk, G.Y., Krivovichev, S., and Burns, P.C. (2002) Cerite-(La), $(La,Ce,Ca)_9(Fe,Ca,Mg)(SiO_4)[SiO_3(OH)]_4(OH)_3$, a new mineral species from the Khibina Alkaline Massif: Occurrence and crystal structure. The Canadian Mineralogist, 40, 1177-1184. DOI: 10.2113/gscanmin.40.4.1177

Pan, Y. and Fleet, M.E. (1990) Halogen-bearing allanite from the White River gold occurrence, Hemlo area, Ontario. The Canadian Mineralogist, 28, 67–75.

Pan, Y. and Fleet, M.E. (1996) Rare earth element mobility during prograde granulite facies metamorphism: significance of fluorine. Contributions to Mineralogy and Petrology, 123, 251–262.

Pan, Y., Fleet, M.E., and Barneti, R.L. (1994) Rare-Earth mineralogy and geochemistry of the Mattagami Lake volcanogenic massive sulfide deposit, Quebec. The Canadian Mineralogist, 32, 133–147.

Pekov, I.V., Pasero, M., Yaskovskaya, A.N., Chukanov, N.V., Pushcharovsky, D.Y., Merlino, S., Zubkova, N.V., Kononkova, N.N., Men'shikov, Y.P., Zadov, A.E. (2007) Fluorcalciobritholite, $(Ca,REE)_5[(Si,P)O_4]_3F$, a new mineral: description and crystal chemistry. European Journal of Mineralogy, 19(1), 95-103. DOI: 10.1127/0935-1221/2007/0019-0095

Peterman, Z.E. and Hedge, C.E. (1968) Chronology of Precambrian events in the Front Range, Colorado. Canadian Journal of Earth Sciences, 5, 749–756.

Peterman, Z.E., Hedge, C.E., and Braddock, W.A. (1968) Age of Precambrian Events in the Northeastern Front Range, Colorado. Journal of Geophysical Research, 73(6), 2277-2296. DOI: 10.1029/JB073i006p02277

Rabbitt, J.C. (1952) Summary of the research work of the trace elements section geochemistry and petrology branch for the period July 1 - September 30, 1951. US Geological Survey report, TEI-182(February 1952), 33 pp.

Ruberti, E., Enrich, G.E.R., and Gomes, C.B. (2008) Hydrothermal REE fluorcarbonate mineralization at Barra Do Itapirapuã, a multiple stockwork carbonatite, Southern Brazil. The Canadian Mineralogist, 46, 901–914.

Rudnick, R.L.and Gao, S. (2003) Composition of the Continental Crust, in: Heinrich, D.H., Turekian, K.K. (Eds.), Treatise on Geochemistry. Elsevier Ltd, pp. 1–64. DOI: 10.1016/B0-08-043751-6/03016-4

Shen, J. and Moore, P.B. (1982) Törnebohmite, $RE_2AI(OH)[SiO_4]_2$: crystal structure and genealogy of RE(III)Si(lV) <=> Ca(II)P(V) isomorphisms. American Mineralogist, 67, 1021-1028.

Simmons, W.B. and Heinrich, E.W. (1980) Rare-Earth pegmatites of the South Platte District, Colorado. Colorado Geological Survey, Resource Series 11, 138 pp.

Simmons, W.B., Lee, M.T., and Brewster, R.H. (1987) Geochemistry and evolution of the South Platte granite-pegmatite system, Jefferson County, Colorado. Geochimica et Cosmochimica Acta, 51(3), 455-471. DOI: 10.1016/0016-7037(87)90061-5

Smith, D.R., Noblett, J., Wobus, R.A., Unruh, D., Douglass, J., Beane, R., Davis, C., Goldman, S., Kay, G., Gustavson, B., Saltoun, B., and Stewart, J. (1999) Petrology and geochemistry of late-stage intrusions of the A-type, mid-Proterozoic Pikes Peak batholith (Central Colorado, USA): implications for petrogenetic models. Precambrian Research, 98(3-4), 271-305. DOI: 10.1016/S0301-9268(99)00049-2

Sørensen, H. (1997) The agpaitic rocks - an overview. Mineralogical Magazine, 61, 485-498. DOI: 10.1180/minmag.1997.061.407.02

Steiger, R.H. and Jäger, E. (1977) Subcommission on geochronology: Convention on the use of decay constants in geo- and cosmochronology. Earth and Planetary Science Letters, 36, 359–362.

Stern, T.W., Phair, G., and Newell, M.F. (1971) Boulder Creek batholith, Colorado part II: Isotopic age of emplacement and morphology of zircon. Geological Society of America Bulletin, 82, 1615-1634. DOI: 10.1130/0016-7606(1971)82[1615:BCBCPI]2.0.CO;2

Tweto, O. (1987) Rock Units of the Precambrian basement in Colorado, 54 pp. U.S. Geological Survey Professional Paper 1321-A.

Tweto, O. (1979) Geologic map of Colorado, special publication, scale 1:500,000. U.S.Geological Survey, Reston, Virginia.

Vasyukova, O. and Williams-Jones, A.E. (2014) Fluoride–silicate melt immiscibility and its role in REE ore formation: Evidence from the Strange Lake rare metal deposit, Québec-

Labrador, Canada. Geochimica et Cosmochimica Acta, 139, 110–130. DOI: 10.1016/j.gca.2014.04.031

Webster, J.D. (1990) Partitioning of F between H2O and CO2 fluids and topaz rhyolite melt Implications for mineralizing magmatic-hydrothermal fluids in F-rich granitic systems. Contributions to Mineralogy and Petrology, 104, 424–438.

Webster, J., Thomas, R., Förster, H.-J., Seltmann, R., and Tappen, C. (2004) Geochemical evolution of halogen-enriched granite magmas and mineralizing fluids of the Zinnwald tin-tungsten mining district, Erzgebirge, Germany. Mineralium Deposita, 39, 452–472.

Wells, J.D. (1967) Geology of the Eldorado Springs quadrangle Boulder and Jefferson counties, Colorado, 91 pp. U.S. Geological Survey Bulletin 1221-D.

Wing, B.A., Ferry, J.M., and Harrison, T.M. (2003) Prograde destruction and formation of monazite and allanite during contact and regional metamorphism of pelites: petrology and geochronology. Contributions to Mineralogy and Petrology, 145(2), 228-250. DOI: 10.1007/s00410-003-0446-1

Wolf, M.B.and London, D. (1995) Incongruent dissolution of REE- and Sr-rich apatite in peraluminous granitic liquids: Differential apatite, monazite, and xenotime solubilities during anatexis. American Mineralogist, 80, 765–775.

Wood, S.A. (1990) The aqueous geochemistry of the rare-earth elements and yttrium 2. Theoretical predictions of speciation in hydrothermal solutions to 350°C at saturation water vapor pressure. Chemical Geology, 88, 99–125.

992

Figure captions

Figure 1: (a) Map of the USA showing the location of map (b). **(b)** General geological setting of the Mesoproterozoic intrusions within the Front Range of Colorado (simplified after Tweto 1979). **(c)** Modified geological map from Cole and Braddock (2009), with locations of the northern (1) and southern (2) localities studied, as originally described by Goddard and Glass (1940).

Figure 2: (a) Detail of 1.2-meter drill core. The characteristic black rim, chiefly made of allanite-(Ce), surrounding the lighter grey fluorite- and fluorbritholite-(Ce)-rich core. **(b)** Outcrop photographs showing the REE-mineralization in pods and veins from the northern locality. **(c,d)** Detail of a more evolved vein showing the dark allanite-(Ce) rim with and without fluorbritholite-(Ce)-bearing core depending on thickness; photos **(c)** taken at the outcrop and **(d)** of float material.

Figure 3: Microphotographs of thin sections showing **(a)** the amoeboidal contact between aplite, and allanite-(Ce)-rich rim of mineralization in a pod, **(b)** the rim-core-rim relation of a thin vein (with corresponding X-ray element map in Figure 6a), and **(c,d)** preferred orientation of allanite-(Ce) perpendicular to the aplite contact.

Figure 4: EDS spectra of all REE-mineral phases and uraninite identified within the studied mineralization.

Figure 5: Round cluster of monazite-(Ce) and fluorite surrounded by Fe-sulfide in the core zone #4.

Figure 6: (a) Whole rock REE analysis of veins normalized to chondrite (McDonough and Sun 1995). **(b)** Whole rock trace element analysis normalized to upper crust (Rudnick and Gao 2003). REE and trace element analyses from Silver Plume-type intrusions are taken from Flanagan (1973) and Anderson and Thomas (1985).

Figure 7: Composite RGB X-ray maps characterizing the variation and spatial relationship of the REE-mineralization. Color code for the mineral assignments for **(a-c)** Si-Ca-La and **(d,e)** Ca-Al-C maps are given on the bottom-right. X = major phase; ± = minor phase. Aln = allanite-(Ce); Kfs = K-feldspar; Mnz = monazite-(Ce); Pl = plagioclase; Qz = quartz; Törn. = törnebohmite-(Ce); F-brit. or F-britholite = fluorbritholite-(Ce). **(a)** X-ray map of a thin vein (from Figure 3b) from rim to rim. Red = Si, green = Ca, blue = La. **(b)** High-resolution detail of rim for region indicated in (a). **(c)** X-ray map of representative core region. **(d,e)** Details of the two rims from mineral zone #3a and #3b. White arrows indicate inclusion of cerite-(Ce) or törnebohmite-(Ce) (= törn.) within core zone #4. Light blue areas are voids in the sample, formed either during sample preparation or through alteration (formation of late REE-carbonate, see discussion). Dashed white arrows on the top-left of **(e)** indicates a late Ca-bearing bastnäsite-(Ce)vein, and the Qz's highlight a late quartz vein. These maps (and additional ones not presented here) were used to calculate the modal abundance of each phase reported in Table 2.

Figure 8: BSE images of allanite-(Ce) illustrating compositional variations. **(a)** Rim area (mineral zone #1) with zoned allanite-(Ce) close to the aplite, and homogeneous allanite-(Ce) composition towards the core of the mineralization highlighted in the inset (mineral zone #2). **(b,c)** Detail of a typical zoned allanite-(Ce) crystal from zone #1 with corresponding analyses summary depicting the increase in REE content from core to intermediate rim, followed by a slight decrease at the very rim. **(d)** Allanite-(Ce) isolated in the aplite.

Figure 9: Variations of $Fe^{2+}/(Fe^{2+}+Mg^{2+}+Mn^{2+})$ ratio versus **(a)** $Fe^{3+}/(Fe^{3+}+Al^{3+})$ ratio and **(b)** Y+REE for zoned allanite-(Ce) isolated in the aplite or within mineral zone #1 and allanite-(Ce) from zone #2. Manganese is assumed to be all Mn^{2+}, whereas Fe^{2+}-Fe^{3+} content is recalculated by charge balance (see details in supplementary material). Core composition of outer rim zone #1 is close to the allanite-(Ce) end-member (point 1) and progressively evolves towards ferriallanite-(Ce) and dissakisite-(Ce) with increasing REE- and Fe^{3+}-content towards the rim (point 2) before evolving back to allanite-(Ce) at the very rim (point 3). The relatively homogeneous (unzoned) allanite-(Ce) from inner rim zone #2 reaches a maximum REE-content around 1 apfu Y+REE (point 4).

Figure 10: (a) X-ray element maps in monazite-(Ce) grains from mineral zone #4. **(b)** Summary of U-Th-Pb dating by electron microprobe analysis of monazite-(Ce). Results are represented using Gaussian probability curves obtained from 5 to 8 individual analyses (2σ errors). "Moacyr" monazite age consistency standard (TIMS $^{207}Pb/^{235}U$ 506.7±1.4 Ma and $^{208}Pb/^{232}U$ 506.4±1.8 Ma; B. Davis, pers. comm. 2005) was analyzed four times

1062 before, during and after the analysis session. **(c)** Summary of U-Th-Pb dating by electron
1063 microprobe analysis of uraninite.
1064
1065 **Figure 11: (a)** La+Ce versus (Other REE)+Ca+Mg+Th+U variation in törnebohmite-(Ce). **(b)**
1066 Y+REE versus Ca+Mg+Sr variation in cerite-(Ce). **(c)** Ce-La-Nd ternary diagram for
1067 bastnäsite-(Ce) analyses. Variations of **(d)** Si versus P and **(e)** Y+REE versus
1068 Ca+Fe+Sr+Mg in fluorbritholite-(Ce).
1069
1070 **Figure 12:** Chondrite-normalized REE-pattern of REE-minerals. **(a)** Averages for each REE-
1071 mineral. **(b-e)** Variations for each REE mineral **(b)** in the rim zone #1 and #2 [allanite-
1072 (Ce), monazite-(Ce)], **(c)** in the intermediate zone #3 [cerite-(Ce), törnebohmite-(Ce)],
1073 **(d)** in the core zone zone #4 [fluorbritholite-(Ce), uraninite], and **(e)** for the pure and Ca-
1074 bearing bastnäsite-(Ce).
1075
1076 **Figure 13:** Ce/Y versus Ce/Nd diagram illustrating the progressive enrichment in Y and Nd
1077 (+HREE) of minerals from zone #1 to #4. A: bulk composition for the allanite-(Ce)-rich
1078 rim; B: averaged bulk rock compositions. Yttrium was chosen instead of a HREE, as
1079 most analyses are below detection limit for most HREE except Y.
1080
1081 **Figure 14:** Proposed petrogenetic model for the mineralization growth. See text for discussion.
1082

Table captions

Table 1: Ideal formula of mineral discussed in the text.

Table 2: Mineral abundance in each four major mineral zones.

NOTES: Minor occurrence of mineral zone #3 and spatial inhomogeneity made it difficult to estimate the modal abundances of minerals in this intermediate zone, as some phases occur only locally and in variable proportion.

Table 3: Whole-rock analyses from REE-mineralization.

NOTES: Oxide values are in weight-%. REE and trace elements are given in ppm. Oxygen content from REE and trace element (row "O" above "total") has been recalculated assuming common oxidation state. Analytical error is estimated to be better than 5% based on duplicate analysis. D.L. = detection limits. LOI = loss on ignition.

Table 4: Summary of electron microprobe analyses for each REE phase identified in the mineralization.

NOTES: Only representative single-point analysis or an average of several homogeneous analyses are given. See text for detail and Supplementary Table 2 for the complete set of analyses. The following conditions were used for the mineral formula recalculation ("OH-group" includes OH, F and Cl anion; see supplementary material for details on H_2O, CO_2 and FeO-Fe_2O_3 recalculations):

- Allanite-(Ce): 12 oxygen atoms, 1 OH-group, 6 cations per formula unit (pfu) at T and M sites, as suggested by Ercit (2002).

- Monazite-(Ce): 4 oxygen atoms pfu.
- Törnebohmite-(Ce): 8 oxygen atoms, 1 OH group pfu.
- Cerite-(Ce): 17 cations, 4 OH groups pfu.
- Bastnäsite-(Ce): 1 oxygen atom, 1 CO_2 group, 1 OH group pfu.
- Uraninite: 1 cation pfu, charge balance (U^{4+}/U^{6+}) assuming structural formula described by Janeczek and Ewing (1992).
- Fluorbritholite-(Ce): 12oxygen atoms, 1 OH group pfu.

"< 0.xx" indicates value below detection limit; "-" indicates an element not analyzed. Based on counting statistics, relative errors are estimated to be <2% at the >10 wt-% level, 2-5% at the 10 to 3 wt-% level, 5-10% at the 3 to 1 wt-% level and >20% at >0.5% level.

Supplementary figure & tables

Supplementary Figure 1: Variations of ratios of $Fe^{2+}/(Fe^{2+}+Mg^{2+})$ versus **(a)** $Fe^{3+}/(Fe^{3+}+Al^{3+}+Mn^{3+})$ and **(b)** Y+HREE for zoned allanite-(Ce). This figure differs from Figure 9 by assuming all manganese is Mn^{3+}.

Supplementary Table 1: Analytical setups for each electron microprobe analysis session including analyzed elements and X-ray lines, standards, peak and background positions, and counting time used.

NOTES: Two slightly different setups were used to include Sr, Cl and Ti analysis during a second analysis session. Each setup was optimized to keep the total analysis time short. To do so, Si and P analysis were analyzed on TAP crystal instead of PET during the second analysis setup; results for Si and P from both setups are identical, although more accurate on TAP due to a higher count rate on this spectrometer. Counting time on each backgrounds was set as half the counting time on peak. Background positions were adequately chosen to avoid interferences.

Supplementary Table 2: Complete set of analyses obtained in each REE-mineral phase.

Figure 1

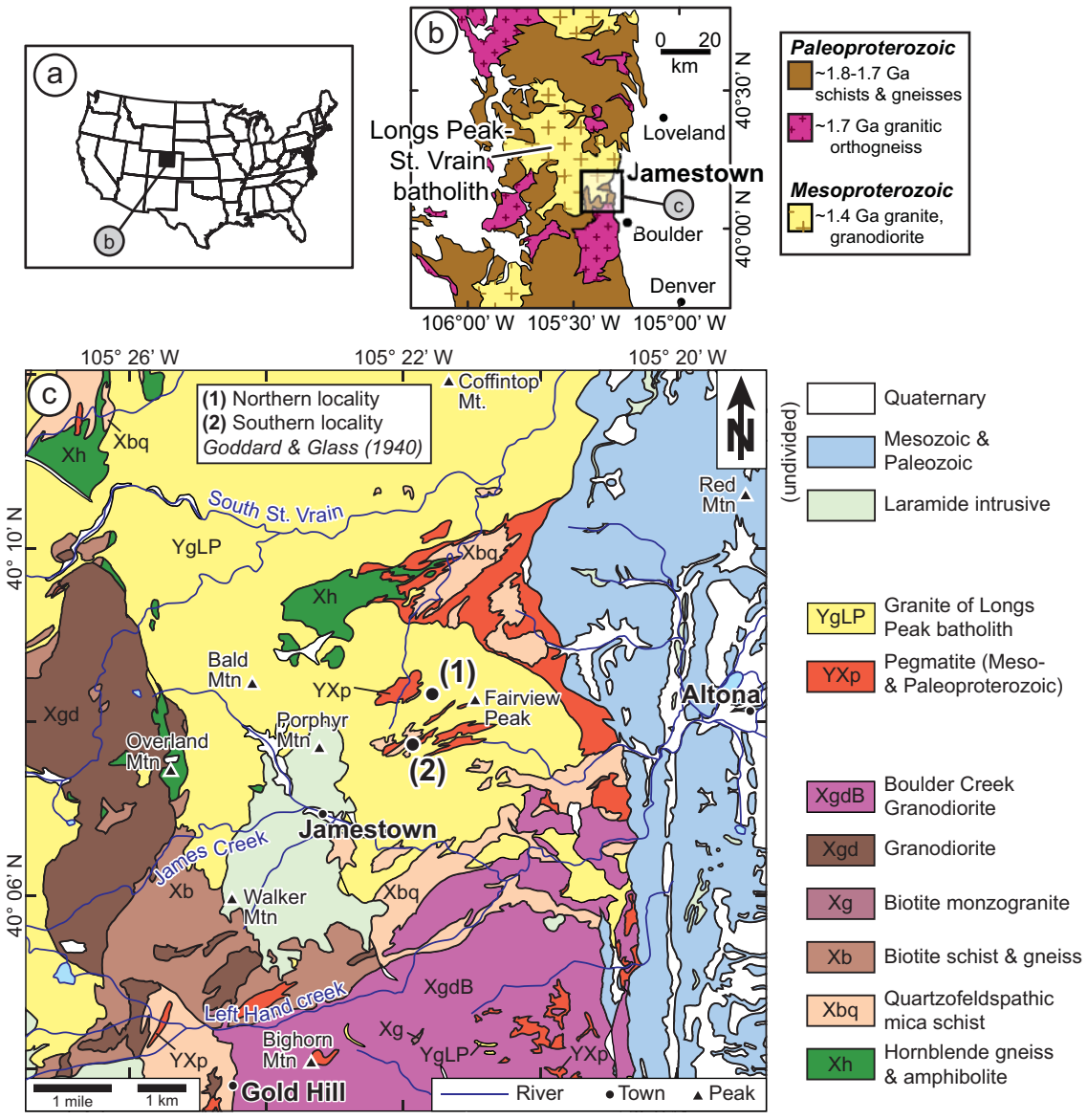
a
b
c
0 20
km
Longs Peak-
St. Vrain
batholith
Loveland
Jamestown
Boulder
Denver
40°30' N
40°00' N
106°00' W
105°30' W
105°00' W
Paleoproterozoic
~1.8-1.7 Ga schists & gneisses
~1.7 Ga granitic orthogneiss
Mesoproterozoic
~1.4 Ga granite, granodiorite
105° 26' W
105° 22' W
105° 20' W
40° 10' N
40° 06' N
(1) Northern locality
(2) Southern locality
Goddard & Glass (1940)
Coffintop Mt.
Red Mtn
South St. Vrain
Bald Mtn
Fairview Peak
Porphyr Mtn
Overland Mtn
Altona
James Creek
Walker Mtn
Left Hand creek
Bighorn Mtn
Gold Hill
1 mile
1 km
River
Town
Peak
(undivided)
Quaternary
Mesozoic & Paleozoic
Laramide intrusive
YgLP Granite of Longs Peak batholith
YXp Pegmatite (Meso- & Paleoproterozoic)
XgdB Boulder Creek Granodiorite
Xgd Granodiorite
Xg Biotite monzogranite
Xb Biotite schist & gneiss
Xbq Quartzofeldspathic mica schist
Xh Hornblende gneiss & amphibolite

Figure 2

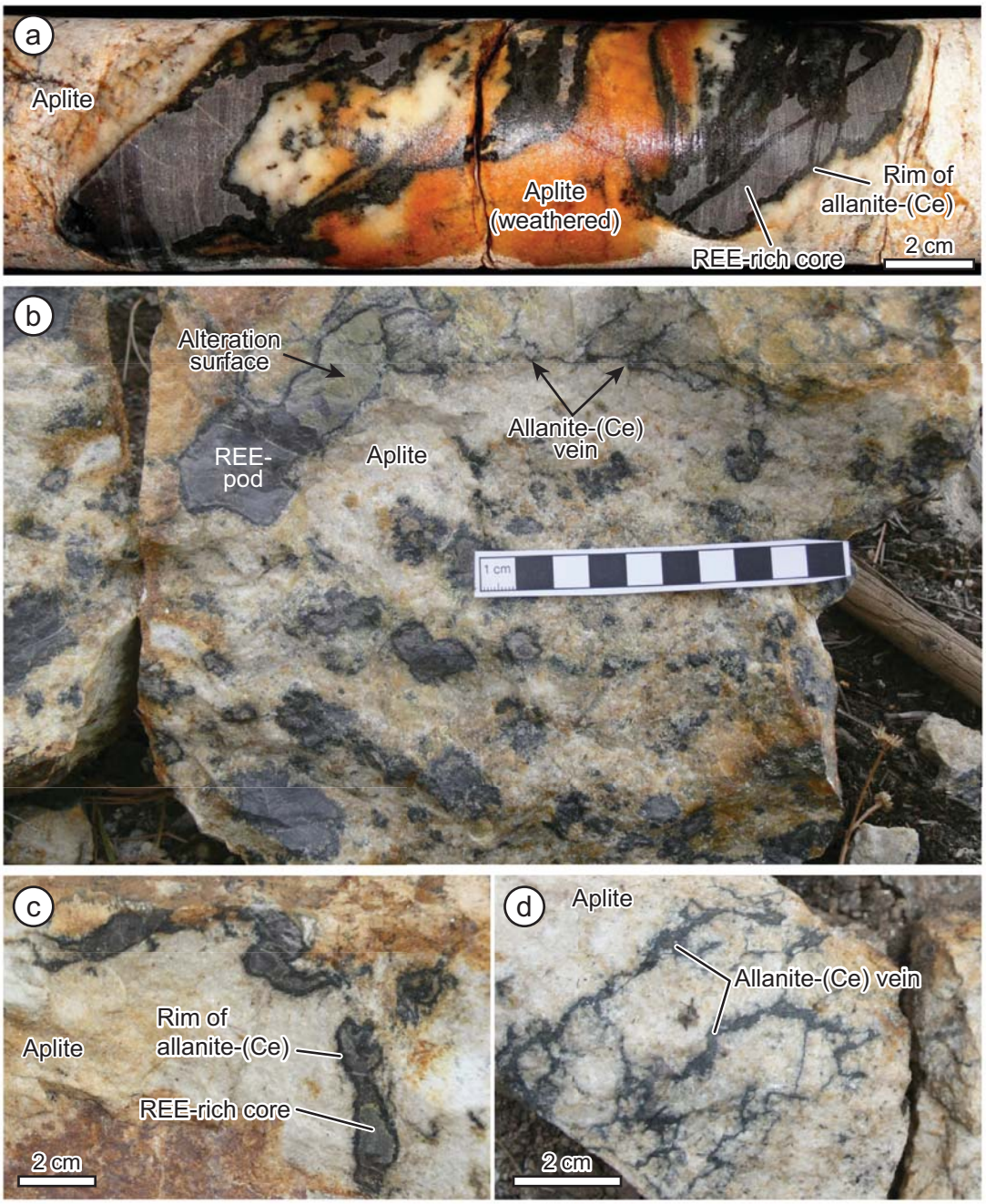
a
Aplite
Aplite
(weathered)
Rim of
allanite-(Ce)
REE-rich core
2 cm
b
Alteration
surface
REE-
pod
Aplite
Allanite-(Ce)
vein
1 cm
c
Aplite
Rim of
allanite-(Ce)
REE-rich core
2 cm
d
Aplite
Allanite-(Ce) vein
2 cm

Figure 3

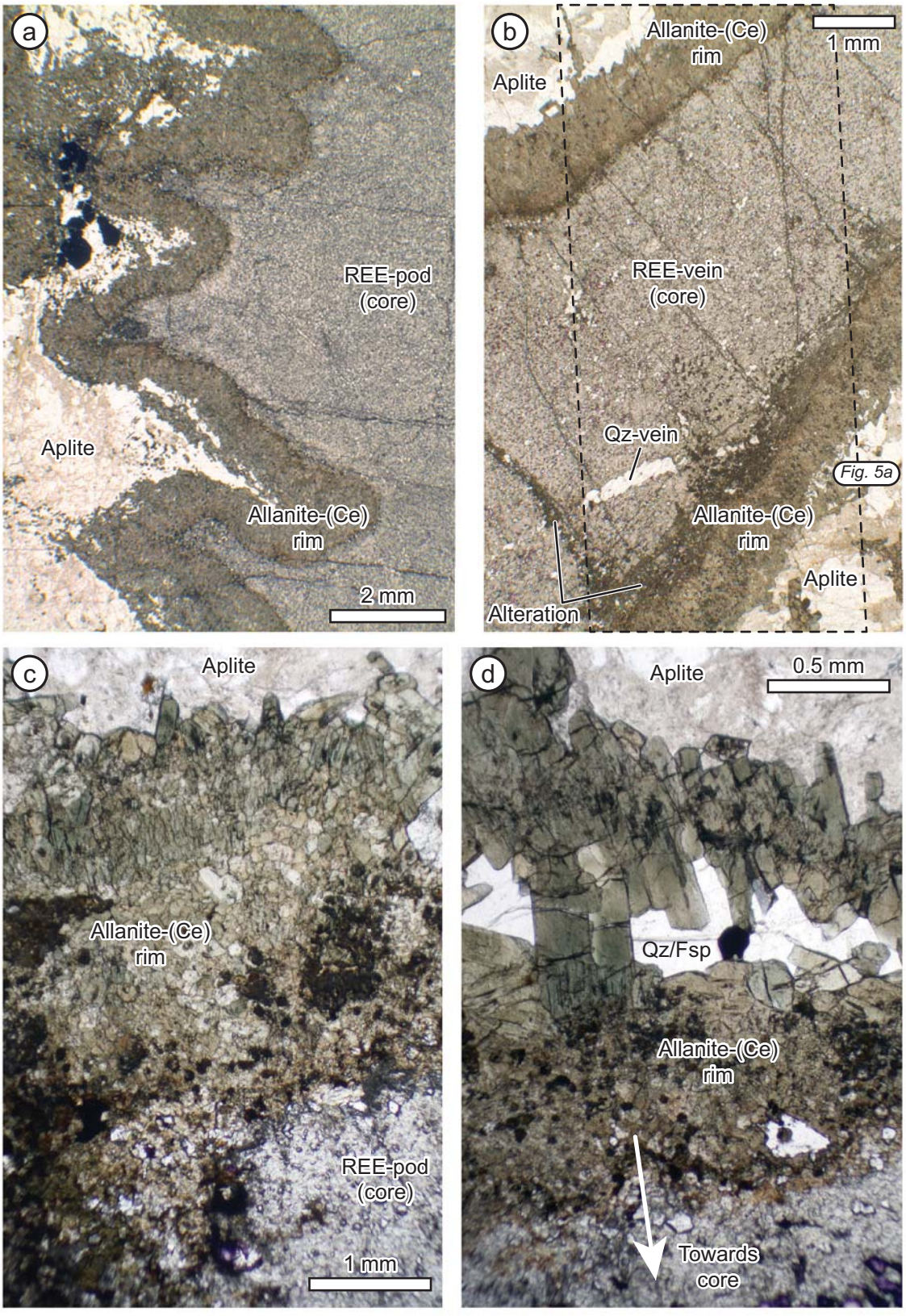
a
REE-pod
(core)
Aplite
Allanite-(Ce)
rim
2 mm
b
Allanite-(Ce)
rim
1 mm
Aplite
REE-vein
(core)
Qz-vein
Fig. 5a
Allanite-(Ce)
rim
Aplite
Alteration
c
Aplite
Allanite-(Ce)
rim
REE-pod
(core)
1 mm
d
Aplite
0.5 mm
Qz/Fsp
Allanite-(Ce)
rim
Towards
core

Figure 4

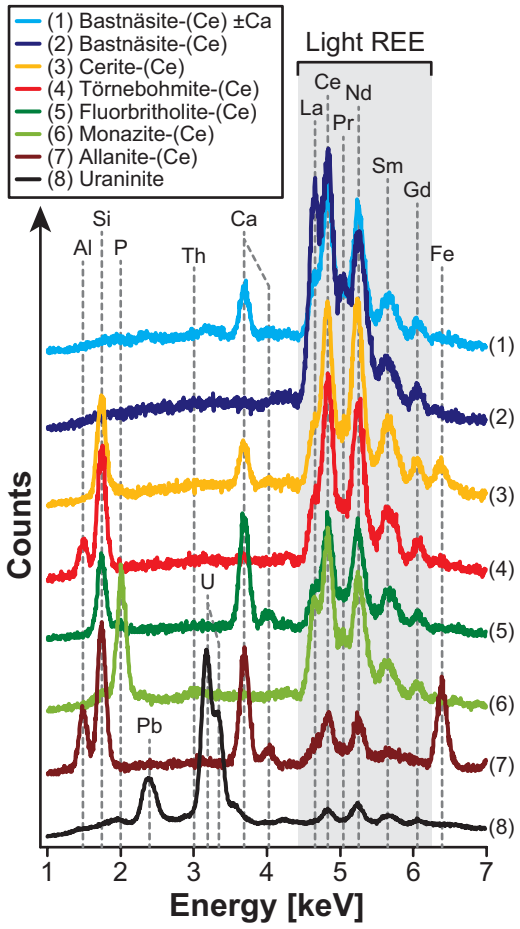
(1) Bastnäsite-(Ce) ±Ca
(2) Bastnäsite-(Ce)
(3) Cerite-(Ce)
(4) Törnebohmite-(Ce)
(5) Fluorbritholite-(Ce)
(6) Monazite-(Ce)
(7) Allanite-(Ce)
(8) Uraninite
Light REE
Ce
Nd
La
Pr
Sm
Gd
Fe
Si
Al
P
Th
Ca
U
Pb
(1)
(2)
(3)
(4)
(5)
(6)
(7)
(8)
Counts
1
2
3
4
5
6
7
Energy [keV]

Figure 5

Figure 6

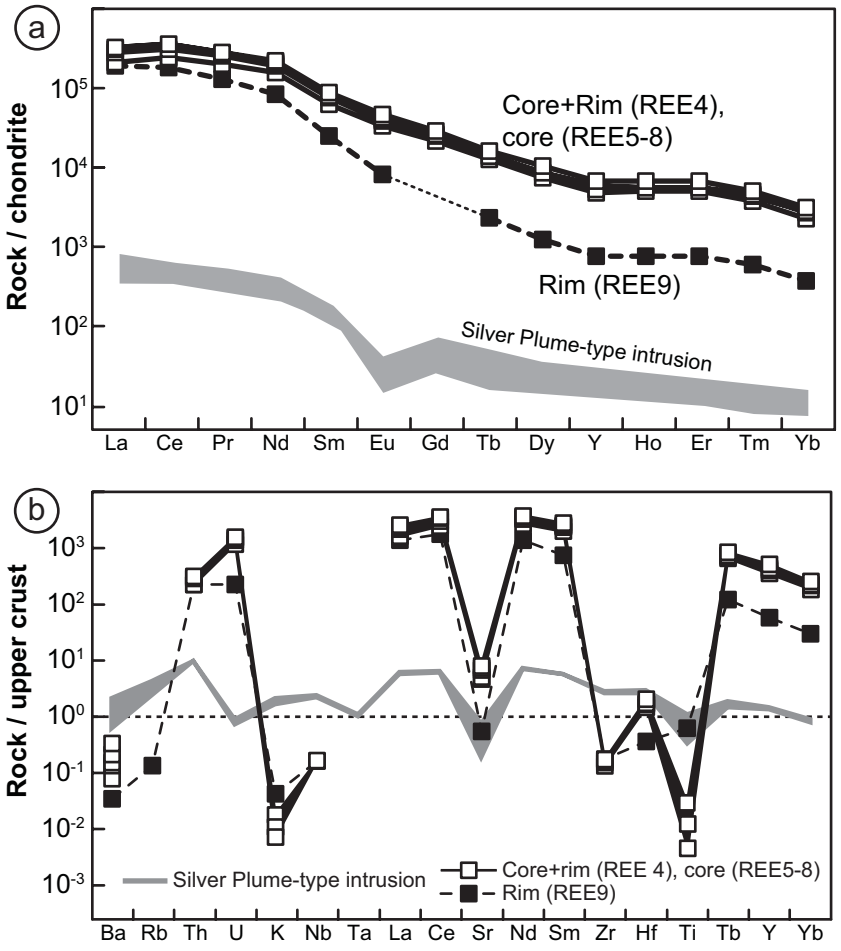
a
Rock / chondrite
10^5
10^4
10^3
10^2
10^1
Core+Rim (REE4),
core (REE5-8)
Rim (REE9)
Silver Plume-type intrusion
La Ce Pr Nd Sm Eu Gd Tb Dy Y Ho Er Tm Yb
b
Rock / upper crust
10^3
10^2
10^1
10^0
10^{-1}
10^{-2}
10^{-3}
Silver Plume-type intrusion
Core+rim (REE 4), core (REE5-8)
Rim (REE9)
Ba Rb Th U K Nb Ta La Ce Sr Nd Sm Zr Hf Ti Tb Y Yb

This is a preprint, the final version is subject to change, of the American Mineralogist (MSA)
Cite as Authors (Year) Title. American Mineralogist, in press.
(DOI will not work until issue is live.) DOI: http://dx.doi.org/10.2138/am-2015-5253

Figure 7

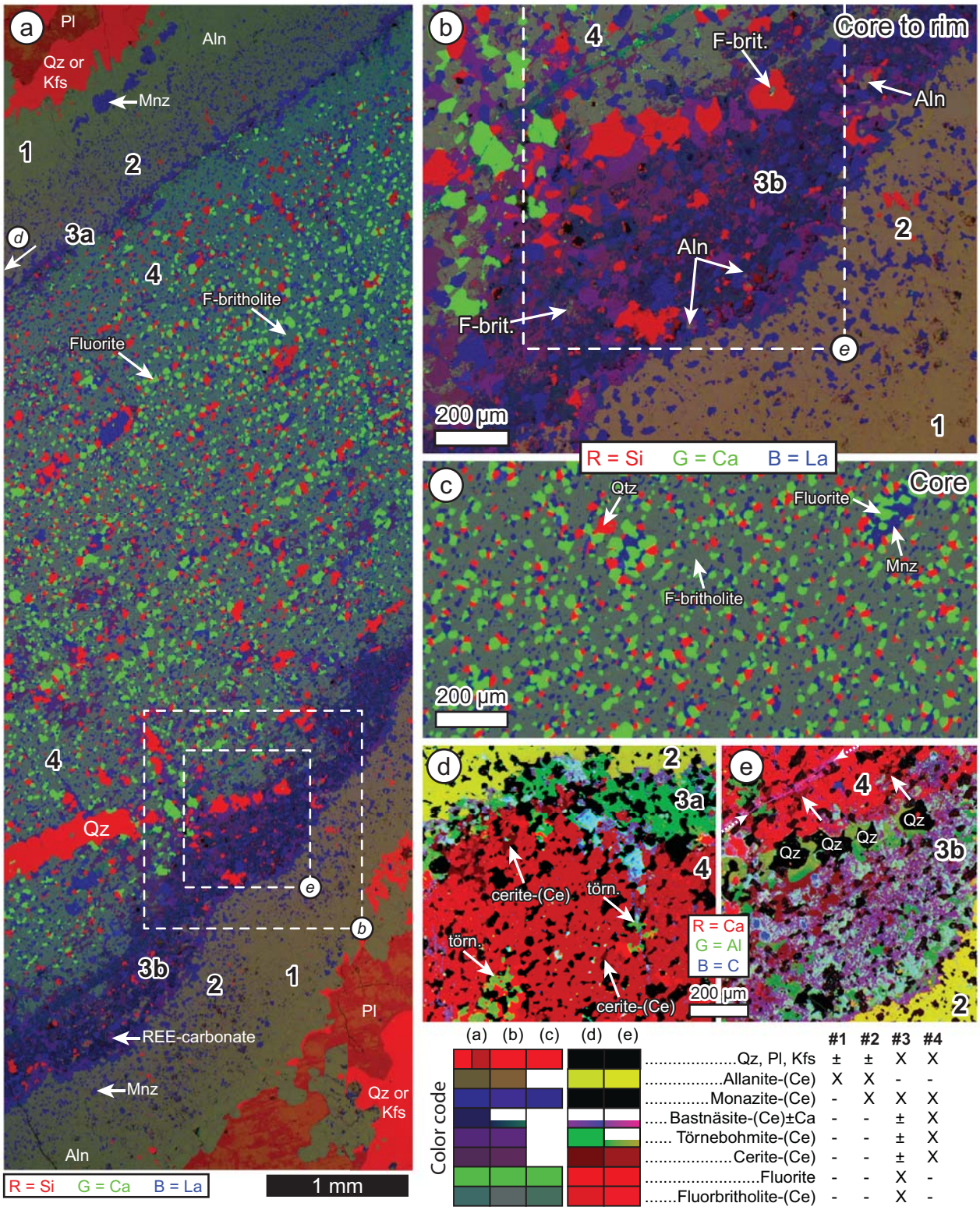

Figure 8

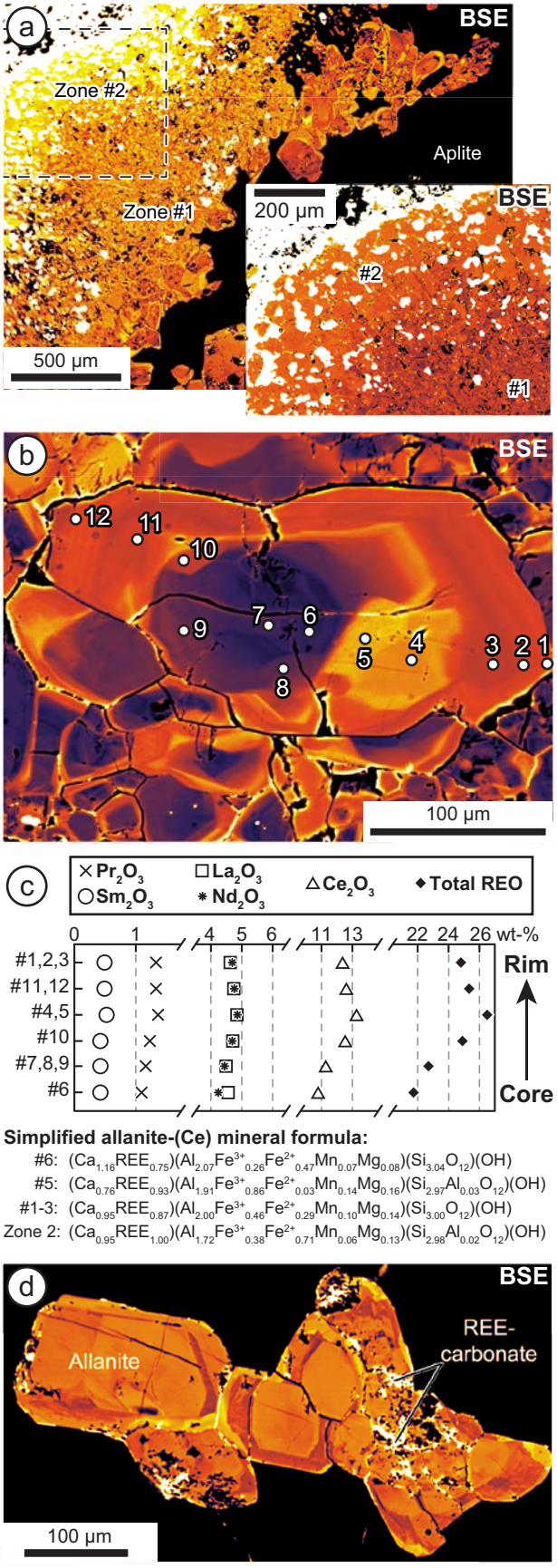
a
BSE
Zone #2
Aplite
Zone #1
200 µm
BSE
#2
#1
500 µm
b
BSE
12
11
10
9
7
6
5
4
3
2
1
8
100 µm
c
Pr2O3
La2O3
Ce2O3
Total REO
Sm2O3
Nd2O3
0 1 4 5 6 11 13 22 24 26 wt-%
#1,2,3
#11,12
#4,5
#10
#7,8,9
#6
Rim
Core
Simplified allanite-(Ce) mineral formula:
#6: (Ca1.16REE0.75)(Al2.07Fe3+0.26Fe2+0.47Mn0.07Mg0.08)(Si3.04O12)(OH)
#5: (Ca0.76REE0.93)(Al1.91Fe3+0.86Fe2+0.03Mn0.14Mg0.16)(Si2.97Al0.03O12)(OH)
#1-3: (Ca0.95REE0.87)(Al2.00Fe3+0.46Fe2+0.29Mn0.10Mg0.14)(Si3.00O12)(OH)
Zone 2: (Ca0.95REE1.00)(Al1.72Fe3+0.38Fe2+0.71Mn0.06Mg0.13)(Si2.98Al0.02O12)(OH)
d
BSE
Allanite
REE-carbonate
100 µm

Figure 9

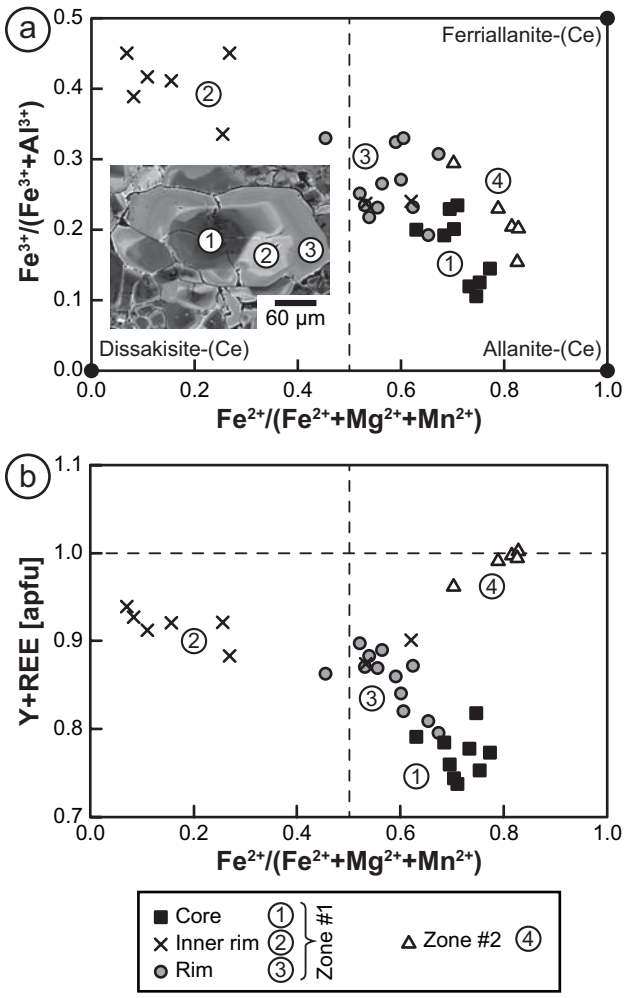
a
Ferriallanite-(Ce)
Dissakisite-(Ce)
Allanite-(Ce)
60 µm
Fe3+/(Fe3++Al3+)
Fe2+/(Fe2++Mg2++Mn2+)
b
Y+REE [apfu]
Fe2+/(Fe2++Mg2++Mn2+)
Core
Inner rim
Rim
Zone #1
Zone #2

Figure 10

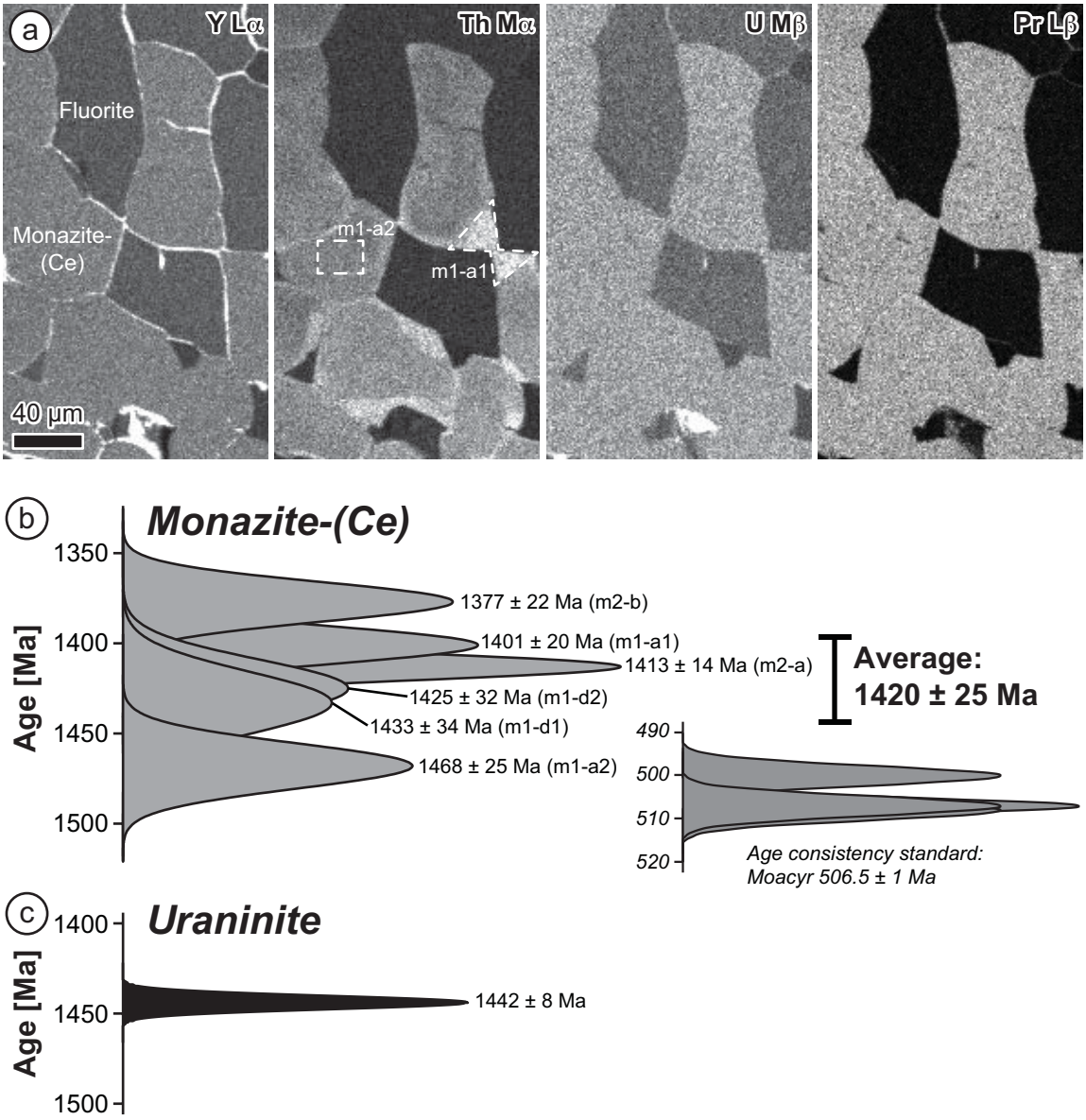
a
Y Lα
Th Mα
U Mβ
Pr Lβ
Fluorite
Monazite-
(Ce)
m1-a2
m1-a1
40 µm
b
Monazite-(Ce)
Age [Ma]
1350
1400
1450
1500
1377 ± 22 Ma (m2-b)
1401 ± 20 Ma (m1-a1)
1413 ± 14 Ma (m2-a)
1425 ± 32 Ma (m1-d2)
1433 ± 34 Ma (m1-d1)
1468 ± 25 Ma (m1-a2)
Average:
1420 ± 25 Ma
490
500
510
520
Age consistency standard:
Moacyr 506.5 ± 1 Ma
c
Uraninite
Age [Ma]
1400
1450
1500
1442 ± 8 Ma

Figure 11

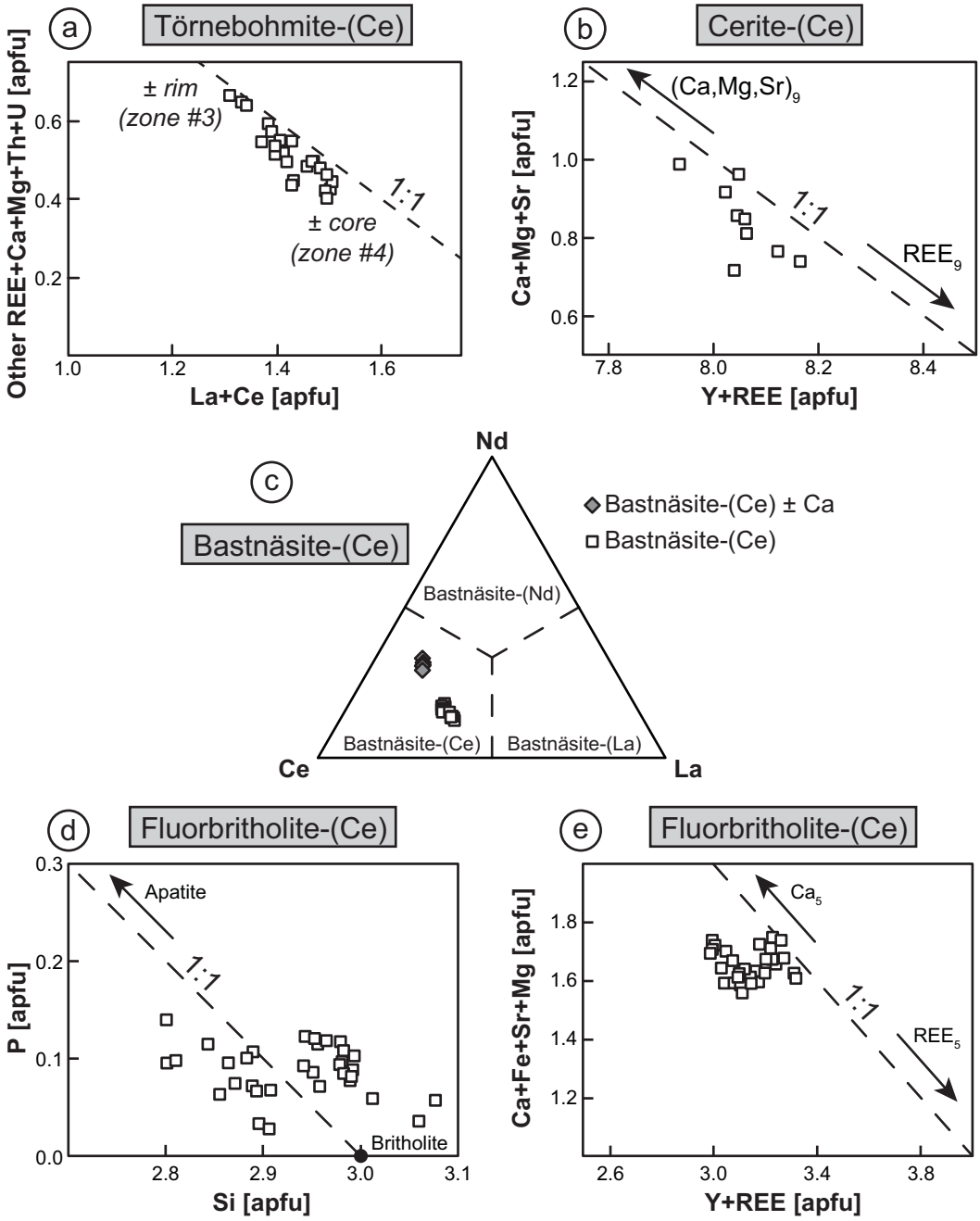
a
Törnebohmite-(Ce)
± rim
(zone #3)
± core
(zone #4)
1:1
Other REE+Ca+Mg+Th+U [apfu]
La+Ce [apfu]
b
Cerite-(Ce)
(Ca,Mg,Sr)9
REE9
1:1
Ca+Mg+Sr [apfu]
Y+REE [apfu]
c
Bastnäsite-(Ce)
Nd
Ce
La
Bastnäsite-(Nd)
Bastnäsite-(Ce)
Bastnäsite-(La)
Bastnäsite-(Ce) ± Ca
Bastnäsite-(Ce)
d
Fluorbritholite-(Ce)
Apatite
1:1
Britholite
P [apfu]
Si [apfu]
e
Fluorbritholite-(Ce)
Ca5
REE5
1:1
Ca+Fe+Sr+Mg [apfu]
Y+REE [apfu]

Figure 12

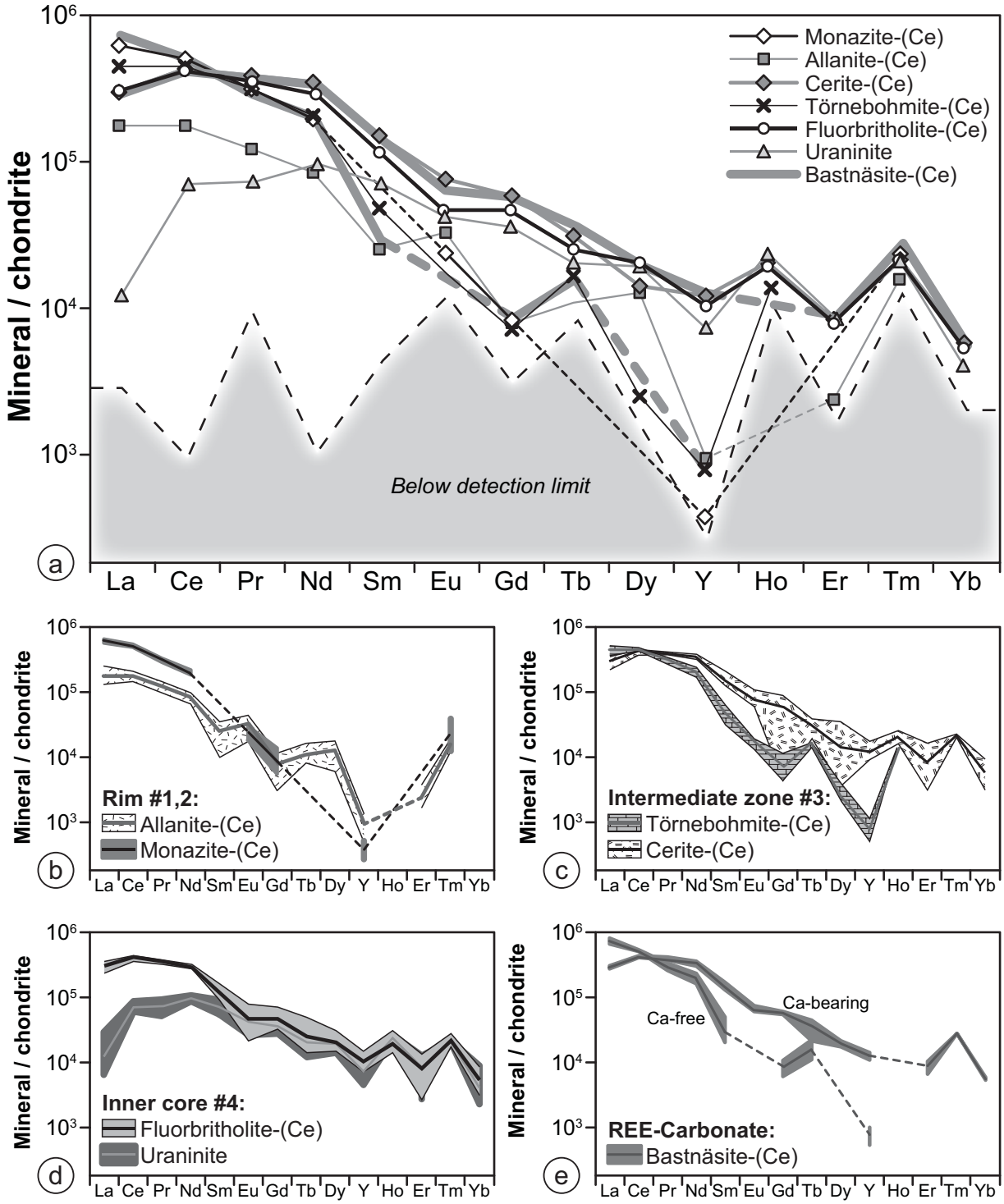
Mineral / chondrite
Monazite-(Ce)
Allanite-(Ce)
Cerite-(Ce)
Törnebohmite-(Ce)
Fluorbritholite-(Ce)
Uraninite
Bastnäsite-(Ce)
Below detection limit
a
La Ce Pr Nd Sm Eu Gd Tb Dy Y Ho Er Tm Yb
Rim #1,2:
Allanite-(Ce)
Monazite-(Ce)
b
Intermediate zone #3:
Törnebohmite-(Ce)
Cerite-(Ce)
c
Inner core #4:
Fluorbritholite-(Ce)
Uraninite
d
Ca-free
Ca-bearing
REE-Carbonate:
Bastnäsite-(Ce)
e

Figure 13

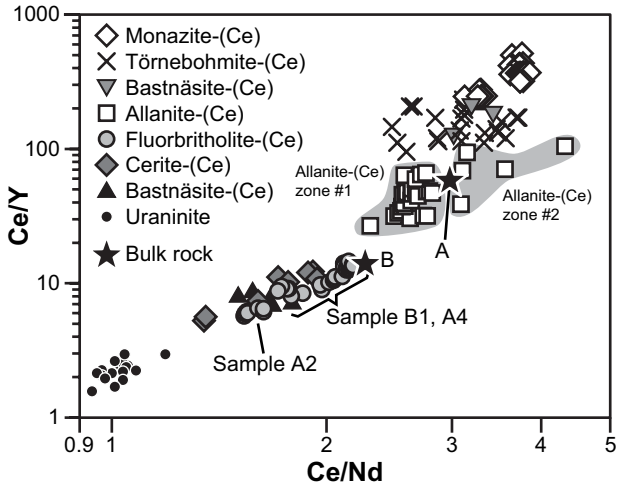
1000
100
10
1
Ce/Y
0.9
1
2
3
4
5
Ce/Nd
Monazite-(Ce)
Törnebohmite-(Ce)
Bastnäsite-(Ce)
Allanite-(Ce)
Fluorbritholite-(Ce)
Cerite-(Ce)
Bastnäsite-(Ce)
Uraninite
Bulk rock
Allanite-(Ce) zone #1
Allanite-(Ce) zone #2
A
B
Sample B1, A4
Sample A2

Figure 14

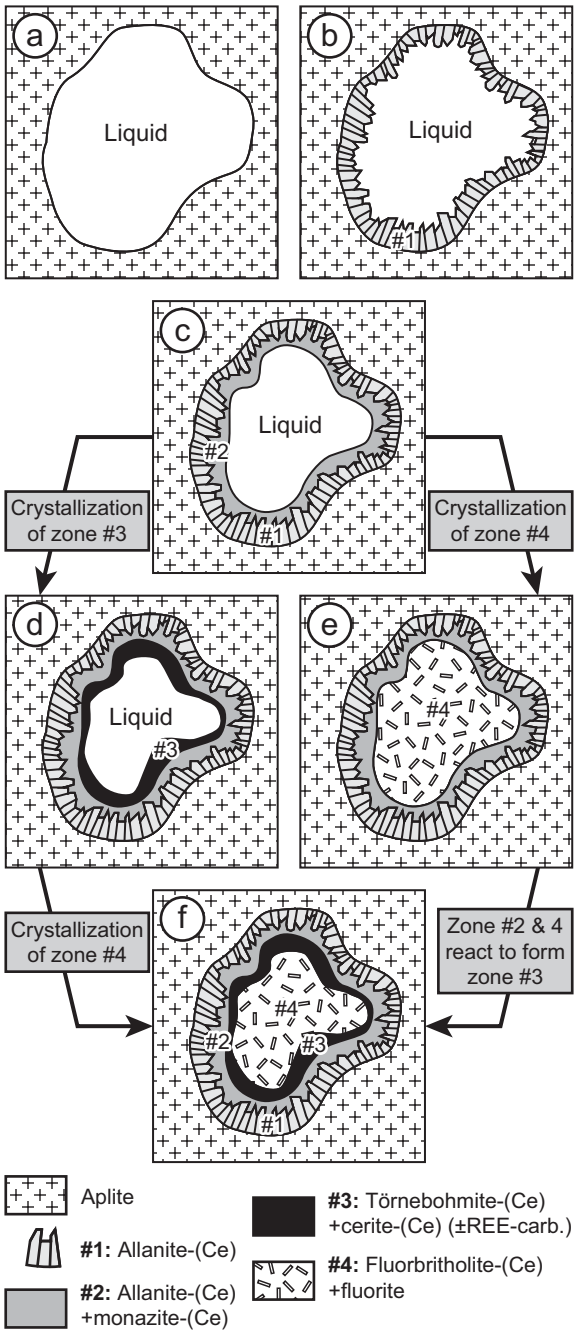
a
Liquid
b
Liquid
#1
c
Liquid
#2
#1
Crystallization of zone #3
Crystallization of zone #4
d
Liquid
#3
e
#4
Crystallization of zone #4
Zone #2 & 4 react to form zone #3
f
#4
#2
#3
#1
Aplite
#1: Allanite-(Ce)
#2: Allanite-(Ce) +monazite-(Ce)
#3: Törnebohmite-(Ce) +cerite-(Ce) (±REE-carb.)
#4: Fluorbritholite-(Ce) +fluorite

Table 1. Ideal formula of mineral discussed in the text.

Mineral	Ideal formula
Allanite-(Ce)	$(Ca,Ce)_2\ (Al,Fe^{3+})_3\ (SiO_4)\ (Si_2O_7)\ O\ (OH)$
Ferriallanite-(Ce)	$Ca\ Ce\ Al\ Fe^{3+}\ Fe^{2+}\ (SiO_4)\ (Si_2O_7)\ O\ (OH)$
Dissakisite-(Ce)	$Ca\ Ce\ Mg\ Al_2\ (SiO_4)\ (Si_2O_7)\ O\ (OH)$
Manganiandrosite-(Ce)	$Mn^{2+}\ Ce\ Mn^{3+}\ Al\ Mn^{2+}\ (SiO_4)\ (Si_2O_7)\ O\ (OH)$
Khristovite-(Ce)	$(Ca,Ce)\ Ce\ Mn^{2+}\ (Mg,Fe^{2+})\ Al\ (SiO_4)\ (Si_2O_7)\ (O,F)\ (OH)$
Piemontite	$Ca_2\ (Mn^{3+},Fe^{3+})\ Al_2\ (SiO_4)\ (Si_2O_7)\ O\ (OH)$
Monazite-(Ce)	$(REE)\ PO_4$
Fluorbritholite-(Ce)	$(Ca,Ce)_5\ (SiO_4)_3\ (F,OH)$
Cerite-(Ce)	$(Ce,Ca)_9\ (Mg,Fe^{3+})\ (SiO_4)_3\ [(SiO_3)\ (OH)]_4\ (OH)_3$
Aluminocerite-(Ce)	$(Ce,Ca)_9\ (Al,Fe^{3+})\ (SiO_4)_3\ [(SiO_3)\ (OH)]_4\ (OH)_3$
Törnebohmite-(Ce)	$Ce_2\ Al\ (SiO_4)_2\ (OH)$
Bastnäsite-(Ce)	$Ce\ CO_3\ (OH,F)$
Synchysite-(Ce)	$Ca\ Ce\ (CO_3)_2\ (OH,F)$
Uraninite	$(U^{4+}_{1-x-y-z},U^{6+}_x,REE^{3+}_y,M^{2+}_z)\ O_{2+x-(0.5y)-z}$

Table 2. Mineral abundance in each four major mineral zones.

	Allanite-(Ce)	Monazite-(Ce)	Fluorbritholite-(Ce)	Cerite-(Ce)	Törnebohmite-(Ce)	Bastnäsite-(Ce)	Uraninite	Quartz	Fluorite
Zone #1	~100%							<0.5%	
Zone #2	80-85%	15-20%						<0.5%	
Zone #3	*Minor*	15-20%	*Minor*	*Major*	*Major*	*Major*	Rare	*Minor*	Rare
Zone #4		12%	70%			<0.5%	0.5%	4%	13%

This is a preprint, the final version is subject to change, of the American Mineralogist (MSA)
Cite as Authors (Year) Title. American Mineralogist, in press.
(DOI will not work until issue is live.) DOI: http://dx.doi.org/10.2138/am-2015-5253

Table 3. Whole-rock analyses from REE-mineralization.

		Core+rim	Core	Core	Core	Core	Rim
	D.L.	**REE4**	**REE5**	**REE6**	**REE7**	**REE8**	**REE9**
SiO_2	*0.01*	21.65	15.26	18.44	18.92	18.51	33.35
Al_2O_3	*0.01*	2.18	1.24	0.29	0.27	0.40	9.26
Fe_2O_3	*0.01*	2.06	1.09	0.25	0.32	0.39	18.32
MnO	*0.001*	0.336	0.289	0.311	0.281	0.298	0.567
MgO	*0.01*	0.07	0.08	0.01	0.02	0.02	0.57
CaO	*0.01*	12.50	27.24	14.57	14.15	14.23	6.46
Na_2O	*0.01*	0.07	0.02	0.02	0.02	0.02	0.06
K_2O	*0.01*	0.05	0.02	0.03	0.03	0.03	0.12
TiO_2	*0.001*	0.019	0.008	0.003	0.003	0.003	0.400
P_2O_5	*0.01*	4.58	3.72	4.55	4.84	4.59	1.59
LOI	-	3.46	4.65	4.37	3.40	3.95	1.57
F	*0.01*	4.72	16.80	7.61	6.19	6.74	0.26
O=F	-	-1.99	-7.07	-3.20	-2.61	-2.84	-0.11
La	*0.1*	67700	50600	79500	78000	73600	45200
Ce	*0.1*	194000	152000	225000	220000	219000	113000
Pr	*0.05*	23400	18800	26600	25600	26100	11900
Nd	*0.1*	87900	72700	98100	94500	99300	39000
Sm	*0.1*	11100	9490	11900	11700	13000	3680
Eu	*0.05*	2220	1920	2360	2320	2700	456
Gd	*0.1*	4920	4220	5170	4970	5800	-
Tb	*0.1*	506	454	506	512	593	83.6
Dy	*0.1*	2090	1850	2090	2090	2590	311
Y	*2*	9154	7512	8500	9226	10690	1220
Ho	*0.1*	305	275	310	312	377	41.7
Er	*0.1*	705	614	720	705	827	95.5
Tm	*0.05*	81.4	68.6	81.1	82.8	94	11
Yb	*0.1*	446	366	436	448	506	60.1
Lu	*0.04*	54.7	46.7	55	56.2	62.3	8.39
Sc	*1*	58	38	57	61	53	36
U	*0.1*	3680	3160	4140	4180	4020	613
Th	*0.1*	3060	2410	3240	3220	3230	2360
Pb	*5*	2350	1340	1920	2080	1880	1040
Sr	*2*	1480	2321	2548	2211	1640	179
Ba	*3*	96	209	50	134	86	23
As	*5*	454	382	473	504	525	214
W	*0.5*	9	11	7	10	9	5
Rb	*2*	b.d.	< 2	< 2	< 2	< 2	11
Nb	*1*	2	2	< 1	< 1	< 1	2
Ta	*25*	< 25	< 25	< 25	< 25	< 25	< 25
Cs	*0.5*	< 0.5	< 0.5	< 0.5	< 0.5	< 0.5	0.9
Be	*1*	6	5	7	7	7	6
V	*5*	11	< 5	< 5	< 5	< 5	539
Cr	*20*	< 20	< 20	< 20	< 20	< 20	< 20
Co	*1*	< 1	< 1	< 1	< 1	< 1	7
Ni	*20*	< 20	< 20	< 20	< 20	< 20	< 20
Cu	*10*	30	10	< 10	< 10	< 10	190
Zn	*30*	60	110	< 30	< 30	< 30	240
Ge	*1*	< 1	< 1	< 1	< 1	< 1	89
Zr	*4*	34	26	32	32	30	36
Mo	*2*	< 2	< 2	< 2	< 2	< 2	< 2
Ag	*0.5*	1	0.8	1.1	1	1.1	< 0.5
In	*0.2*	< 0.2	< 0.2	< 0.2	< 0.2	< 0.2	< 0.2
Sn	*1*	2	2	< 1	< 1	< 1	28
Sb	*0.5*	< 0.5	< 0.5	< 0.5	< 0.5	< 0.5	< 0.5
Hf	*0.2*	8.8	7.8	9	9.1	10.9	1.9
Tl	*0.1*	< 0.1	< 0.1	< 0.1	< 0.1	< 0.1	< 0.1
Bi	*0.4*	104	84.2	108	115	127	1.6
O	-	*7.11*	*5.66*	*8.09*	*7.92*	*7.99*	*3.78*
Total	**-**	**98.42**	**102.11**	**102.74**	**100.06**	**101.02**	**98.27**

This is a preprint, the final version is subject to change, of the American Mineralogist (MSA)
Cite as Authors (Year) Title. American Mineralogist, in press.
(DOI will not work until issue is live.) DOI: http://dx.doi.org/10.2138/am-2015-5253

Table 4. Summary of electron microprobe analyses for each REE phase ide

	Allanite-(Ce)							
Sample	***B1***	***A2***	***A2***	***B1***	***B1***	***A2***	***A2***	***B1***
Domain	***Core***	***Rim out***	***Rim in***	***Core***	***Rim out***	***Rim in***	***Rim in***	***All***
Zone	***Aplite***	***Aplite***	***Aplite***	***#1***	***#1***	***#1***	***#1***	***#2***
# points	2	3	1	7	2	8	7	5
SiO_2	31.66	32.41	31.75	32.66	32.38	32.16	31.85	30.24
TiO_2	0.09	0.11	0.11	*n.d.*	*n.d.*	*n.d.*	*n.d.*	0.15
P_2O_5	*< 0.03*	*< 0.03*	*< 0.03*	*< 0.03*	*< 0.03*	*< 0.03*	*< 0.03*	*< 0.03*
SO_3	*< 0.02*	*< 0.04*	*< 0.04*	*< 0.02*	*< 0.02*	*< 0.02*	*< 0.02*	*< 0.02*
Al_2O_3	17.74	18.04	17.25	18.79	18.24	18.04	17.69	14.98
Fe_2O_3	2.89	7.66	10.32	3.88	5.21	5.37	7.94	3.97
Mn_2O_3	-	-	-	-	-	-	-	-
FeO	7.08	4.79	2.73	6.57	5.78	5.13	3.32	9.57
MnO	1.27	1.03	1.46	1.00	1.06	1.27	1.51	0.67
MgO	0.63	0.62	0.79	0.62	0.92	1.01	1.16	0.85
CaO	10.62	9.96	8.37	11.36	10.49	9.35	8.32	9.01
Na_2O	0.25	0.07	0.15	0.04	0.06	0.13	0.19	0.05
K_2O	*< 0.07*	*n.d.*	*n.d.*	*< 0.07*	*< 0.07*	*< 0.07*	*< 0.07*	*< 0.07*
SrO	0.24	*< 0.07*	*< 0.07*	*n.d.*	*n.d.*	*n.d.*	*n.d.*	*< 0.06*
La_2O_3	3.72	4.61	4.41	4.41	4.37	4.82	5.09	6.73
Ce_2O_3	10.57	12.08	12.82	10.89	12.11	12.59	13.32	14.67
Pr_2O_3	1.27	1.40	1.59	1.13	1.30	1.37	1.39	1.31
Nd_2O_3	4.53	4.40	5.12	4.22	4.61	4.82	5.03	3.70
Sm_2O_3	0.50	0.45	0.48	0.43	0.48	0.46	0.48	0.22
Eu_2O_3	0.21	0.23	0.14	0.24	0.21	0.23	0.16	0.22
Gd_2O_3	0.17	0.15	0.22	0.22	0.17	0.19	0.17	0.08
Tb_2O_3	*< 0.04*	0.05	*< 0.04*	0.04	0.05	*< 0.04*	*< 0.03*	*< 0.04*
Dy_2O_3	0.45	0.39	0.49	0.32	0.34	0.39	0.45	0.23
Y_2O_3	0.25	0.18	0.22	0.22	0.15	0.18	0.18	0.12
Ho_2O_3	*< 0.06*	*< 0.06*	*< 0.06*	*< 0.06*	*< 0.06*	*< 0.06*	*< 0.06*	*< 0.06*
Er_2O_3	*< 0.03*	0.05	*< 0.03*	0.04	*< 0.03*	0.04	0.04	*< 0.03*
Tm_2O_3	*< 0.03*	*< 0.03*	*< 0.03*	*< 0.03*	*< 0.03*	*< 0.03*	*< 0.03*	*< 0.03*
Yb_2O_3	*< 0.03*	*< 0.03*	*< 0.03*	*< 0.03*	*< 0.03*	*< 0.03*	*< 0.03*	*< 0.03*
ThO_2	0.20	0.07	0.10	0.09	0.08	0.07	0.06	*< 0.06*
UO_2	*< 0.05*	*< 0.04*	*< 0.04*	*< 0.05*	*< 0.05*	*< 0.05*	*< 0.05*	*< 0.05*
PbO	*n.d.*	*n.d.*	*n.d.*	*n.d.*	*n.d.*	*n.d.*	*n.d.*	*n.d.*
H_2O	1.46	1.63	1.61	1.62	1.62	1.61	1.61	1.52
F	*< 0.08*	*< 0.08*	*< 0.09*	*< 0.10*	*< 0.09*	*< 0.09*	*< 0.09*	*< 0.08*
Cl	0.59	*< 0.01*	*< 0.01*	*n.d.*	*n.d.*	*n.d.*	*n.d.*	*< 0.01*
O=F,Cl	-0.13	-	-	-	-	-	-	-
TOTAL	**96.26**	**100.37**	**100.13**	**98.79**	**99.65**	**99.25**	**99.95**	**98.27**
REO %	21.67	23.98	25.49	22.16	23.80	25.10	26.30	27.28

Si	3.027	2.977	2.948	3.015	2.993	2.999	2.964	2.983
P	-	-	-	-	-	-	-	-
S	-	-	-	-	-	-	-	-
Al (T)	-	0.023	0.052	-	0.007	0.001	0.036	0.017
Sum T	***3.027***	***3.000***	***3.000***	***3.015***	***3.000***	***3.000***	***3.000***	***3.000***
Al (M2)	1.000	1.000	1.000	1.000	1.000	1.000	1.000	1.000
Sum M2	***1.000***	***1.000***	***1.000***	***1.000***	***1.000***	***1.000***	***1.000***	***1.000***
Al (M1)	0.993	0.931	0.835	1.000	0.980	0.982	0.905	0.725
Ti	0.007	0.008	0.008	-	-	-	-	0.011
Fe^{3+} (M1)	-	0.062	0.157	-	0.020	0.018	0.095	0.264
Sum M1	***1.000***	***1.000***	***1.000***	***1.000***	***1.000***	***1.000***	***1.000***	***1.000***
Al (M3)	0.006	-	-	0.045	-	-	-	-
Fe^{3+} (M3)	0.322	0.557	0.693	0.357	0.435	0.471	0.594	0.093
Mn^{3+}	-	-	-	-	-	-	-	-
Fe^{2+}	0.452	0.278	0.083	0.420	0.354	0.288	0.126	0.727
Mn^{2+}	0.102	0.080	0.115	0.078	0.083	0.100	0.119	0.056
Mg	0.090	0.084	0.109	0.086	0.127	0.140	0.162	0.125
Sum M3	***0.973***	***1.000***	***1.000***	***0.985***	***1.000***	***1.000***	***1.000***	***1.000***
Ca (A2)	0.201	0.172	0.114	0.229	0.173	0.121	0.084	-
La	0.131	0.156	0.151	0.150	0.149	0.166	0.175	0.245
Ce	0.370	0.406	0.436	0.368	0.410	0.430	0.454	0.530
Pr	0.044	0.047	0.054	0.038	0.044	0.047	0.047	0.047
Nd	0.155	0.144	0.170	0.139	0.152	0.161	0.167	0.130
Sm	0.034	0.030	0.032	0.029	0.032	0.031	0.032	0.016
Eu	0.015	0.015	0.009	0.016	0.014	0.015	0.011	0.016
Gd	0.005	0.005	0.007	0.007	0.005	0.006	0.005	0.003
Tb	-	0.001	-	0.001	0.002	-	-	-
Dy	0.014	0.011	0.015	0.009	0.010	0.012	0.013	0.007
Y	0.013	0.009	0.011	0.011	0.008	0.009	0.009	0.006
Ho	-	-	-	-	-	-	-	-
Er	-	0.002	-	0.001	-	0.001	0.001	-
Tm	-	-	-	-	-	-	-	-
Yb	-	-	-	-	-	-	-	-
Sr	0.014	-	-	-	-	-	-	-
Th	0.004	0.002	0.002	0.002	0.002	0.002	0.001	-
U	-	-	-	-	-	-	-	-
Pb	-	-	-	-	-	-	-	-
Sum A2	***1.000***	***1.000***	***1.000***	***1.000***	***1.000***	***1.000***	***1.000***	***1.000***
Ca (A1)	0.887	0.808	0.719	0.894	0.866	0.813	0.746	0.952
Na	0.047	0.012	0.026	0.007	0.011	0.023	0.034	0.010
K	-	-	-	-	-	-	-	-
Sum A1	***0.934***	***0.820***	***0.745***	***0.902***	***0.877***	***0.836***	***0.779***	***0.962***
Vacancy	*0.066*	*0.180*	*0.255*	*0.098*	*0.123*	*0.164*	*0.221*	*0.038*
O	12.000	12.000	12.000	12.000	12.000	12.000	12.000	12.000
TOTAL	**7.934**	**7.820**	**7.745**	**7.902**	**7.877**	**7.836**	**7.779**	**7.962**
OH	0.932	1.000	1.000	1.000	1.000	1.000	1.000	1.000
F	-	-	-	-	-	-	-	-
Cl	0.069	-	-	-	-	-	-	-
REE	0.781	0.826	0.884	0.769	0.825	0.877	0.914	1.000
Ce/Nd	2.39	2.82	2.57	2.64	2.70	2.67	2.72	4.06
Ce/Y	28.96	47.28	39.41	34.77	54.45	49.02	52.21	84.89
La/Yb	-	-	-	-	-	-	-	-
La/Dy	9.45	13.68	10.35	15.86	14.72	14.14	12.99	34.09
Dy/Yb	-	-	-	-	-	-	-	-
Y/Dy	0.92	0.75	0.76	1.12	0.74	0.75	0.65	0.87

Table 4. Continued.

	Monazite-(Ce)					
Sample	***A2***	***A2***	***A2***	***A2***	***A2***	***A2***
Domain	***m1-a1***	***m1-a2***	***m1-d1***	***m1-d2***	***m2-a***	***m2-b***
Zone	***#4***	***#4***	***#4***	***#4***	***#4***	***#4***
# points	6	8	8	6	8	10
Age [My]	**1409**	**1468**	**1430**	**1428**	**1414**	**1380**
Error 2 s	20	25	34	32	14	22
SiO_2	3.07	2.90	2.51	2.14	2.80	2.35
P_2O_5	22.97	23.02	24.59	25.15	24.45	24.47
SO_3	3.39	3.71	3.01	2.62	2.98	2.88
CaO	0.74	0.47	0.40	0.45	0.36	0.45
K_2O	*< 0.02*	*< 0.02*	*< 0.02*	*< 0.02*	*< 0.02*	*< 0.02*
SrO	0.11	0.11	0.06	0.06	0.02	0.14
La_2O_3	16.87	17.59	17.75	17.83	16.06	17.73
Ce_2O_3	36.86	37.46	36.94	36.56	35.88	37.34
Pr_2O_3	3.38	3.37	3.32	3.22	3.47	3.32
Nd_2O_3	10.39	10.26	10.14	9.98	11.23	10.13
Sm_2O_3	*< 0.06*	*< 0.06*	*< 0.06*	*< 0.06*	*< 0.06*	*< 0.06*
Eu_2O_3	0.16	0.17	0.17	0.18	0.15	0.14
Gd_2O_3	*< 0.13*	0.19	0.20	0.21	0.19	0.17
Tb_2O_3	*< 0.03*	*< 0.03*	*< 0.03*	*< 0.03*	*< 0.03*	*< 0.03*
Dy_2O_3	*< 0.03*	*< 0.03*	*< 0.03*	*< 0.03*	*< 0.03*	*< 0.03*
Y_2O_3	0.06	0.06	0.07	0.07	0.10	0.07
Ho_2O_3	*< 0.06*	*< 0.06*	*< 0.06*	*< 0.06*	*< 0.06*	*< 0.06*
Er_2O_3	*< 0.03*	*< 0.03*	*< 0.03*	*< 0.03*	*< 0.03*	*< 0.03*
Tm_2O_3	*< 0.03*	*< 0.03*	0.06	*< 0.03*	0.07	0.05
Yb_2O_3	*< 0.04*	*< 0.04*	*< 0.04*	*< 0.04*	*< 0.04*	*< 0.04*
ThO_2	1.73	0.78	0.49	0.78	1.74	0.76
UO_2	0.10	0.10	0.09	0.10	0.10	0.10
PbO	0.13	0.07	0.05	0.07	0.13	0.07
TOTAL	**99.96**	**100.25**	**99.82**	**99.42**	**99.73**	**100.18**
REO %	67.71	69.10	68.64	68.05	67.15	68.95

Si	0.121	0.114	0.098	0.084	0.110	0.092
P	0.768	0.766	0.815	0.838	0.811	0.815
S	0.101	0.109	0.088	0.077	0.088	0.085
Ca	0.031	0.020	0.017	0.019	0.015	0.019
K	-	-	-	-	-	-
Sr	0.003	0.003	0.001	0.001	0.000	0.003
La	0.246	0.255	0.256	0.259	0.232	0.257
Ce	0.533	0.539	0.529	0.527	0.515	0.538
Pr	0.049	0.048	0.047	0.046	0.050	0.048
Nd	0.147	0.144	0.142	0.140	0.157	0.142
Sm	-	-	-	-	-	-
Eu	0.002	0.002	0.002	0.002	0.002	0.002
Gd	-	0.002	0.002	0.003	0.002	0.001
Tb	-	-	-	-	-	-
Dy	-	-	-	-	-	-
Y	0.001	0.001	0.001	0.001	0.002	0.001
Ho	-	-	-	-	-	-
Er	-	-	-	-	-	-
Tm	-	-	0.001	-	0.001	0.000
Yb	-	-	-	-	-	-
Th	0.016	0.007	0.004	0.007	0.016	0.007
U	0.001	0.001	0.001	0.001	0.001	0.001
Pb	0.001	0.001	0.001	0.001	0.001	0.001
TOTAL	**2.020**	**2.013**	**2.007**	**2.007**	**2.002**	**2.013**
O	4.000	4.000	4.000	4.000	4.000	4.000
REE	0.978	0.993	0.981	0.979	0.961	0.990
Ce/Nd	3.64	3.74	3.73	3.76	3.28	3.78
Ce/Y	423.18	428.02	362.62	358.32	247.39	365.82
La/Yb	-	-	-	-	-	-
La/Dy	-	-	-	-	-	-
Dy/Yb	-	-	-	-	-	-
Y/Dy	-	-	-	-	-	-

Table 4. Continued.

	Törnebohmite-(Ce)				Cerite-(Ce)			Bastnäsite-(Ce)			Bast. ±Ca	
Sample	***A2, B1***	***B1***	***A4***	***A4***	***A2***	***B1***	***B1***	***A2***	***A2***	***A2+A4***	***A4***	***B1***
Domain	*-*	*-*	*-*	*-*	*-*	*-*	*-*	*-*	*-*	*-*	*-*	*-*
Zone	***#3***	***#3***	***#3***	***#4***	***#3***	***#3***	***#3***	***near #4***	***#4***	***#4***	***#4***	***near #4***
# points	***10***	***3***	***7***	***5***	***3***	***3***	***3***	***3***	***5***	***6***	***3***	***2***
SiO_2	25.20	24.68	25.17	25.12	23.55	24.30	23.98	*< 0.05*	*< 0.05*	*< 0.05*	0.95	0.33
TiO_2	*< 0.04*	*< 0.04*	0.12	*< 0.06*	*< 0.04*	*< 0.04*	*< 0.04*	-	*< 0.06*	*< 0.06*	*< 0.06*	*< 0.06*
P_2O_5	*< 0.05*	*< 0.05*	0.20	0.18	*< 0.07*	*< 0.07*	*< 0.07*	*< 0.03*	*< 0.03*	*< 0.03*	0.51	0.54
SO_3	*< 0.02*	*< 0.02*	0.09	*< 0.02*	*< 0.06*	*< 0.06*	*< 0.06*	*< 0.02*	*< 0.02*	*< 0.02*	0.24	1.78
Al_2O_3	10.17	9.80	9.76	9.69	0.19	0.49	0.25	*< 0.06*	*< 0.06*	*< 0.06*	0.15	0.79
Fe_2O_3	0.49	1.01	0.60	0.47	3.05	2.41	3.07	-	-	-	-	-
Mn_2O_3	*< 0.03*	*< 0.03*	0.07	*< 0.04*	0.11	0.41	0.18	-	-	-	-	-
FeO	-	-	-	-	-	-	-	*< 0.03*	*< 0.03*	*< 0.03*	0.30	0.12
MnO	-	-	-	-	-	-	-	0.04	*< 0.04*	*< 0.04*	0.09	*< 0.04*
MgO	0.17	< 0.03	0.22	*0.27*	0.21	0.25	0.13	*< 0.03*	*< 0.06*	*< 0.06*	*< 0.06*	*< 0.06*
CaO	0.33	0.06	1.19	0.27	2.22	2.52	2.31	0.05	0.03	0.04	2.78	1.62
Na_2O	*< 0.04*	*< 0.04*	*< 0.05*	*< 0.05*	*< 0.05*	*< 0.05*	*< 0.05*	*< 0.03*	*< 0.08*	*< 0.08*	*< 0.08*	*< 0.08*
K_2O	*< 0.16*	-	-	-	-	-	-	*< 0.10*	-	-	-	-
SrO	*< 0.09*	*< 0.09*	*< 0.07*	*< 0.07*	*< 0.10*	*< 0.10*	*< 0.10*	-	*< 0.17*	*< 0.17*	*< 0.17*	*< 0.17*
La_2O_3	13.03	14.15	11.51	14.65	9.40	6.48	8.14	19.13	18.74	21.96	8.34	7.77
Ce_2O_3	34.13	34.82	32.62	34.53	32.32	27.63	30.90	36.84	37.98	37.56	30.24	29.74
Pr_2O_3	3.44	3.23	3.49	3.15	4.26	4.30	4.35	3.40	3.32	2.95	3.84	4.37
Nd_2O_3	11.03	9.51	12.18	9.87	17.32	20.04	18.72	11.56	11.15	9.35	17.02	18.45
Sm_2O_3	0.75	0.55	0.95	0.65	2.29	3.33	2.57	0.66	0.51	0.44	2.39	2.78
Eu_2O_3	*< 0.09*	*< 0.09*	0.11	*< 0.10*	0.45	0.65	0.42	*< 0.09*	*< 0.09*	*< 0.09*	0.42	0.45
Gd_2O_3	0.17	0.12	0.19	0.16	*< 0.08*	1.34	1.39	0.19	*< 0.08*	*< 0.08*	1.31	1.31
Tb_2O_3	*< 0.05*	*< 0.05*	*< 0.05*	*< 0.05*	*< 0.05*	0.15	0.11	0.07	*< 0.05*	*< 0.05*	0.09	0.17
Dy_2O_3	*< 0.04*	*< 0.04*	0.08	*< 0.05*	0.11	0.75	0.61	*< 0.05*	*< 0.05*	*< 0.05*	0.54	0.60
Y_2O_3	0.16	0.14	0.16	0.20	1.91	3.35	2.28	0.16	*< 0.10*	*< 0.10*	2.76	2.33
Ho_2O_3	*< 0.08*	*< 0.08*	*< 0.08*	*< 0.08*	*< 0.08*	0.16	*< 0.08*	*< 0.08*	*< 0.12*	*< 0.12*	*< 0.12*	*< 0.12*
Er_2O_3	*< 0.03*	*< 0.04*	*< 0.04*	*< 0.04*	0.09	0.22	0.16	*< 0.03*	*< 0.03*	*< 0.03*	0.18	0.15
Tm_2O_3	*< 0.03*	*< 0.04*	*< 0.04*	*< 0.04*	*< 0.04*	*< 0.04*	*< 0.04*	*< 0.03*	*< 0.06*	*< 0.06*	*< 0.06*	*< 0.06*
Yb_2O_3	*< 0.03*	*< 0.04*	*< 0.04*	*< 0.04*	*< 0.05*	0.15	0.09	*< 0.03*	*< 0.06*	*< 0.06*	0.11	*< 0.06*
ThO_2	0.38	0.23	0.48	0.47	0.20	0.11	0.14	*< 0.04*	*< 0.13*	*< 0.13*	0.19	*< 0.13*
UO_2	*< 0.05*	*< 0.05*	*< 0.06*	*< 0.06*	*< 0.05*	*< 0.05*	*< 0.05*	*< 0.05*	*< 0.05*	*< 0.05*	0.49	0.75
CO_2	-	-	-	-	-	-	-	19.31	19.25	19.42	21.77	22.87
H_2O	1.80	1.80	1.65	1.83	1.42	1.33	1.35	1.53	-	0.14	0.70	2.56
F	*< 0.07*	*< 0.07*	0.40	-	1.08	1.30	1.24	5.10	8.33	8.23	7.93	4.49
Cl	0.13	*< 0.02*	-	-	*< 0.02*	*< 0.02*	*< 0.02*	-	-	-	-	*< 0.03*
O=F,Cl	-0.03	-	-0.17	-	-0.45	-0.55	-0.53	-2.15	-3.51	-3.46	-3.34	-1.89
TOTAL	**101.36**	**100.10**	**101.10**	**101.49**	**99.70**	**101.10**	**101.86**	**95.89**	**95.81**	**96.63**	**99.99**	**102.01**
REO %	62.71	62.52	61.25	63.08	68.14	68.54	69.75	72.01	71.81	72.28	67.23	68.08

Si	2.059	2.051	2.047	2.056	7.283	7.264	7.261	-	-	-	0.032	0.011
Ti	-	-	0.007	-	-	-	-	-	-	-	-	-
P	-	-	0.014	0.012	-	-	-	-	-	-	0.015	0.015
S	-	-	0.005	-	-	-	-	-	-	-	0.006	0.043
Al	0.979	0.960	0.936	0.935	0.069	0.171	0.088	-	-	-	0.006	0.030
Fe^{3+}	0.030	0.063	0.037	0.029	0.711	0.541	0.699	-	-	-	-	-
Mn^{3+}	-	-	0.004	-	0.025	0.094	0.041	-	-	-	-	-
Fe^{2+}	-	-	-	-	-	-	-	-	-	-	0.008	0.003
Mn^{2+}	-	-	-	-	-	-	-	0.001	-	-	0.003	-
Mg	0.021	-	0.027	0.033	0.095	0.109	0.057	-	-	-	-	-
Ca	0.029	0.005	0.104	0.024	0.736	0.806	0.750	0.002	0.001	0.002	0.100	0.056
Na	-	-	-	-	-	-	-	-	-	-	-	-
K	-	-	-	-	-	-	-	-	-	-	-	-
Sr	-	-	-	-	-	-	-	-	-	-	-	-
La	0.393	0.434	0.345	0.442	1.072	0.715	0.909	0.268	0.264	0.306	0.104	0.092
Ce	1.021	1.060	0.971	1.035	3.659	3.024	3.426	0.512	0.531	0.520	0.373	0.348
Pr	0.102	0.098	0.103	0.094	0.480	0.468	0.480	0.047	0.046	0.041	0.047	0.051
Nd	0.322	0.282	0.354	0.289	1.913	2.140	2.025	0.157	0.152	0.126	0.205	0.211
Sm	0.021	0.016	0.027	0.018	0.512	0.719	0.563	0.009	0.007	0.006	0.028	0.031
Eu	-	-	0.003	-	0.100	0.138	0.092	-	-	-	0.005	0.005
Gd	0.005	0.003	0.005	0.004	-	0.133	0.139	0.002	-	-	0.015	0.014
Tb	-	-	-	-	-	0.015	0.011	0.001	-	-	0.001	0.002
Dy	-	-	0.002	-	0.011	0.072	0.060	-	-	-	0.006	0.006
Y	0.007	0.006	0.007	0.009	0.314	0.533	0.368	0.003	-	-	0.049	0.040
Ho	-	-	-	-	-	0.015	-	-	-	-	-	-
Er	-	-	-	-	0.008	0.021	0.016	-	-	-	0.002	0.002
Tm	-	-	-	-	-	-	-	-	-	-	-	-
Yb	-	-	-	-	-	0.013	0.008	-	-	-	0.001	-
Th	0.007	0.004	0.009	0.009	0.014	0.007	0.009	-	-	-	0.001	-
U	-	-	-	-	-	-	-	-	-	-	0.004	0.005
TOTAL	**4.995**	**4.983**	**5.008**	**4.989**	**17.000**	**17.000**	**17.000**	**1.001**	**1.000**	**1.001**	**1.009**	**0.962**
O	8.000	8.000	8.000	8.000	26.720	26.631	26.711	1.000	1.000	1.000	1.000	1.000
C	-	-	-	-	-	-	-	1.000	1.000	1.000	1.000	1.000
OH	0.982	1.000	0.897	1.000	2.947	2.771	2.812	0.388	-	0.016	0.156	0.546
F	-	-	0.103	-	1.053	1.229	1.188	0.612	1.005	0.984	0.844	0.454
Cl	0.018	-	-	-	-	-	-	-	-	-	-	-
Vacancy	0.005	0.017	-	0.011	-	-	-	-		-	-	0.038
REE	1.870	1.899	1.818	1.891	8.068	8.006	8.096	0.998	0.999	0.999	0.834	0.800
Ce/Nd	3.17	3.75	2.75	3.59	1.91	1.41	1.69	3.27	3.49	4.12	1.82	1.65
Ce/Y	146.66	171.18	140.17	118.81	11.66	5.67	9.31	158.37	-	-	7.54	8.78
La/Yb	-	-	-	-	-	53.5	109.4	-	-	-	91.6	-
La/Dy	-	-	164.4	-	100.9	9.9	15.3	-	-	-	17.7	14.8
Dy/Yb	-	-	-	-	-	5.4	7.2	-	-	-	5.2	-
Y/Dy	-	-	3.3	-	29.5	7.4	6.2	-	-	-	8.4	6.4

Table 4. Continued.

	Uraninite		Fluorbritholite						
Sample	***A2***	***A4***	***B1***	***B1***	***B1***	***A2***	***A4***	*Affholter*	*Kartashov*
Domain	***-***	***-***	***-***	***-***	***-***	***-***	***-***	*(1987)*	*(2011)*
Zone	***#4***	***#4***	***near #3***	***near #3***	***#4***	***#4***	***#4, Trn****	*by WDS*	*by EDS*
# points	6	5	***2***	***8***	***11***	***6***	***6***	***-***	***-***
Age [My]	**1439**	**1444**							
Error 2 s	10	9							
SiO_2	*< 0.02*	*< 0.02*	22.90	22.07	20.48	22.74	22.56	21.4	21.11
TiO_2	-	-	*< 0.04*	*< 0.04*	*< 0.04*	-	-	-	-
P_2O_5	-	-	0.91	0.77	0.62	0.98	0.80	1.4	-
SO_3	-	-	*< 0.06*	*< 0.06*	*< 0.06*	*< 0.02*	-	-	-
Al_2O_3	*< 0.02*	*< 0.02*	*< 0.03*	*< 0.03*	*< 0.03*	*< 0.06*	-	-	0.28
Fe_2O_3	*< 0.02*	*< 0.02*	0.50	0.46	0.13	0.27	0.25	0.4	-
Mn_2O_3	*< 0.02*	*< 0.02*	0.49	0.39	0.39	0.59	0.55	-	-
MgO	-	-	*< 0.03*	*< 0.03*	*< 0.03*	*< 0.03*	-	-	-
CaO	0.36	0.22	10.68	10.63	10.68	11.53	10.93	10.6	10.80
Na_2O	-	-	*< 0.05*	*< 0.05*	*< 0.05*	*< 0.04*	-	-	-
K_2O	-	-	-	-	-	*< 0.16*	-	-	-
SrO	-	-	*< 0.10*	0.18	0.33	-	0.19	-	-
La_2O_3	0.36	0.41	8.13	9.06	9.36	6.72	8.03	10.5	9.51
Ce_2O_3	5.06	5.14	28.94	30.05	30.46	26.14	29.13	29.7	29.09
Pr_2O_3	0.82	0.84	3.85	3.84	3.79	3.79	3.87	3.0	3.72
Nd_2O_3	5.02	5.06	16.32	15.10	14.55	16.96	16.13	13.6	14.67
Sm_2O_3	1.23	1.29	2.29	1.87	1.71	2.62	2.22	1.3	0.19
Eu_2O_3	0.24	0.33	0.34	0.28	0.25	0.44	0.35	-	-
Gd_2O_3	0.79	0.83	1.17	0.94	0.87	1.49	1.15	0.6	-
Tb_2O_3	0.06	0.11	0.13	0.09	0.09	0.15	0.10	-	-
Dy_2O_3	0.51	0.60	0.71	0.52	0.46	0.79	0.62	-	0.38
Y_2O_3	1.36	1.64	2.42	1.96	1.55	2.94	2.20	2.6	1.37
Ho_2O_3	*< 0.08*	0.15	*< 0.08*	*< 0.08*	*< 0.08*	0.15	0.09	-	-
Er_2O_3	0.11	0.18	0.19	0.14	0.10	0.21	0.15	-	-
Tm_2O_3	*< 0.05*	*< 0.05*	*< 0.04*	*< 0.04*	*< 0.04*	0.06	0.07	-	-
Yb_2O_3	0.06	0.11	0.12	0.08	0.08	0.14	0.11	-	-
ThO_2	2.34	1.93	0.15	0.13	*< 0.08*	0.12	0.15	0.2	0.43
UO_2	46.62	45.28	0.09	0.15	*< 0.06*	0.16	0.24	0.3	-
UO_3	18.47	17.96	-	-	-	-	-	-	-
PbO	14.41	14.01	-	-	-	-	-	-	-
H_2O	-	-	0.31	0.30	0.22	0.23	0.00	-	-
F	-	-	1.79	1.73	1.80	1.94	2.92	2.5	8.44
Cl	-	-	-	-	-	-	-	-	-
O=F,Cl	-	-	-0.75	-0.73	-0.76	-0.82	-1.23	-1.0	-
TOTAL	**97.82**	**96.09**	**101.63**	**99.99**	**97.16**	**100.33**	**101.56**	**97.1**	**99.99**
REO %	15.60	16.64	64.59	63.99	63.27	62.60	64.10	61.3	58.93

Si	-	-	2.980	2.948	2.867	2.972	2.965	2.910	3.034
Ti	-	-	-	-	-	-	-	-	-
P	-	-	0.100	0.087	0.073	0.108	0.089	0.161	-
S	-	-	-	-	-	-	-	-	-
Al IV	-	-	-	-	-	-	-	-	-
Al VI	-	-	-	-	-	-	-	-	0.047
Fe^{3+}	-	-	0.049	0.046	0.014	0.027	0.025	0.045	-
Mn^{3+}	-	-	0.049	0.040	0.042	0.059	0.055	-	-
Mg	-	-	-	-	-	-	-	-	-
Ca	0.016	0.010	1.489	1.521	1.602	1.615	1.539	1.544	1.663
Na	-	-	-	-	-	-	-	-	-
K	-	-	-	-	-	-	-	-	-
Sr	-	-	-	0.014	0.027	-	0.014	-	-
La	0.005	0.006	0.390	0.446	0.483	0.324	0.389	0.525	0.504
Ce	0.074	0.077	1.379	1.469	1.561	1.251	1.402	1.480	1.530
Pr	0.012	0.012	0.183	0.187	0.193	0.181	0.185	0.151	0.195
Nd	0.072	0.074	0.758	0.720	0.727	0.792	0.757	0.659	0.753
Sm	0.017	0.018	0.103	0.086	0.082	0.118	0.101	0.061	0.009
Eu	0.003	0.005	0.015	0.013	0.012	0.020	0.016	-	-
Gd	0.011	0.011	0.050	0.042	0.040	0.065	0.050	0.026	-
Tb	0.001	0.002	0.006	0.004	0.004	0.006	0.004	-	-
Dy	0.007	0.008	0.030	0.022	0.021	0.033	0.026	-	0.018
Y	0.029	0.036	0.168	0.139	0.115	0.205	0.154	0.188	0.105
Ho	-	0.002	-	-	-	0.006	0.004	-	-
Er	0.001	0.002	0.008	0.006	0.004	0.009	0.006	-	-
Tm	-	-	-	-	-	0.002	0.003	-	-
Yb	0.001	0.001	0.005	0.003	0.003	0.006	0.004	-	-
Th	0.022	0.018	0.004	0.004	-	0.004	0.004	0.006	0.014
U^{4+}	0.417	0.411	0.003	0.004	-	0.005	0.007	0.009	-
U^{6+}	0.156	0.154	-	-	-	-	-	-	-
Pb	0.156	0.154	-	-	-	-	-	-	-
TOTAL	**1.000**	**1.000**	**7.767**	**7.802**	**7.872**	**7.806**	**7.800**	**7.766**	**7.872**
O	1.678	1.496	12.000	12.000	12.000	12.000	12.000	12.000	12.000
OH	-	-	0.263	0.269	0.203	0.198	-	-	-
F	-	-	0.737	0.731	0.797	0.802	1.214	1.075	3.836
Cl	-	-	-	-	-	-	-	-	-
Vacancy	-	-	0.233	0.198	0.128	0.194	0.200	0.234	0.128
REE	0.245	0.250	3.094	3.138	3.248	3.016	3.101	3.090	3.114
Ce/Nd	1.03	1.04	1.82	2.04	2.15	1.58	1.85	2.25	2.03
Ce/Y	2.56	2.16	8.23	10.55	13.52	6.12	9.11	7.87	14.61
La/Yb	7.56	4.61	81.97	136.90	141.71	58.06	88.26	-	-
La/Dy	0.81	0.79	13.11	19.95	23.30	9.74	14.83	-	28.65
Dy/Yb	9.38	5.81	6.25	6.86	6.08	5.96	5.95	-	-
Y/Dy	4.36	4.55	5.63	6.23	5.57	6.15	5.86	-	5.96